FORSCHUNGSZENTRUM KARLSRUHE

Technik und Umwelt

Wissenschaftliche Berichte

FZKA 6694

STELLAR NEUTRON CAPTURE CROSS SECTIONS OF THE Xe ISOTOPES

K. WISSHAK, R. REIFARTH, F. VOSS, and F. KÄPPELER,

Institut für Kernphysik

Forschungszentrum Karlsruhe GmbH, Karlsruhe
2001

ABSTRACT

The (n,γ) cross sections of the important *s*-process nuclei ^{128}Xe, ^{129}Xe, and ^{130}Xe have been measured for the first time in the astrophysically relevant neutron energy range from 3 to 225 keV. Neutrons were produced via the ^{7}Li$(p,n)^{7}$Be reaction by bombarding metallic Li targets with the pulsed proton beam of the Karlsruhe 3.7 MV Van de Graaff accelerator. Highly enriched Xe gas samples in thin-walled titanium spheres were used in the experiment, and capture events were registered with the Karlsruhe 4π Barium Fluoride Detector. The cross sections were determined relative to the gold standard with overall uncertainties of 1.5 - 2.5% over most of the investigated energy range. From these results Maxwellian averaged stellar (n,γ) cross sections with typical uncertainties of 2% were calculated for thermal energies between kT = 8 keV and 100 keV. In contrast to previous theoretical estimates, which were known to exhibit uncertainties of 30 to 50%, this work provides a reliable basis for quantitative astrophysical analyses.

ZUSAMMENFASSUNG

DIE STELLAREN (n,γ) QUERSCHNITTE DER Xe ISOTOPE

Die (n,γ)-Querschnitte der wichtigen s-Prozess-Kerne ^{128}Xe, ^{129}Xe und ^{130}Xe wurden erstmals im astrophysikalisch relevanten Energiebereich von 3 bis 225 keV gemessen. Die Neutronen wurden über die $^{7}\mathrm{Li}(p,n)^{7}$Be-Reaktion durch Beschuss metallischer Li-Targets mit dem gepulsten Protonenstrahl des Karlsruher 3.7 MV Van de Graaff Beschleunigers erzeugt. Im Experiment wurden hochangereicherte Xe-Gasproben in dünnwandigen Titankugeln verwendet. Einfangereignisse wurden mit dem Karlsruher 4π Barium Fluorid Detektor nachgewiesen. Die Querschnitte wurden relativ zum Standard-Querschnitt von Gold bestimmt, wobei im grössten Teil des untersuchten Energiebereichs Unsicherheiten von 1.5 - 2.5% erreicht wurden. Mit diesen Ergebnissen konnten die Maxwell-gemittelten, stellaren (n,γ)-Querschnitte für thermische Energien von $kT = 8$ keV bis 100 keV mit einer Genauigkeit von etwa 2% festgelegt werden. Im Gegensatz zu bisher verfügbaren, theoretischen Abschätzungen, die Unsicherheiten von 30 bis 50% aufwiesen, stellen die Ergebnisse dieser Arbeit eine zuverlässige Grundlage für quantitative, astrophysikalische Analysen dar.

Contents

1 INTRODUCTION

Measurements of neutron capture cross sections with the Karlsruhe 4πBaF$_2$ detector for applications in nuclear astrophysics are now available since more than ten years [1]. During this period all aspects of the method have been studied in detail resulting in continuous improvements and in the implementation of new features. The possibility for achieving uncertainties of $\approx$1% is well established and has been demonstrated for about 50 isotopes. These data had a great impact on the recent update of a cross section compilation for nucleosynthesis studies [2]. With this background it became possible to address difficult problems in nucleosynthesis which are completely out of reach for other experimental approaches.

A prominent example of this type was the first experimental determination of the neutron capture cross section of ^{180m}Ta, the rarest stable isotope in nature [3]. While normally sample masses of $\approx$1 g of highly enriched material are required in such measurements, the world supply of enriched ^{180m}Ta consists of only 150 mg with an enrichment of only 5.5%. That a successful measurement could be performed on that difficult sample illustrates the superior sensitivity of the technique which was recently complemented by extensive computer simulations [4, 5] using the GEANT software [6].

Also in the present experiment, which is the first attempt to use this detector for measurements on noble gas isotopes, sample preparation was the main difficulty, requiring the development of optimized high pressure gas samples. These first measurements on xenon are important since Xe is one of the six elements with two *s*-only isotopes: ^{128}Xe and ^{130}Xe are commonly assigned to the *s* process. Four elements of this group (Te,Ba,Sm,Gd) have already been investigated with the Karlsruhe 4πBaF$_2$ detector [7, 8, 9, 10], while the remaining case is Kr, another noble gas element.

The previous investigations have shown that these examples are important for analyses of branchings in the *s*-process reaction path provided that the stellar (n,γ) cross sections of the involved *s*-only isotopes are known with high accuracy. Such analyses provide constraints on the physical conditions of the *s*-process environment, e.g. on temperature, neutron flux, and electron density. With the present xenon data, also the fifth branching with two *s*-only isotopes belonging to the main component of the *s* process can now be studied. The elements of the main component between Zr and Hg are believed to be produced during helium shell burning of low mass stars in the so-called asymptotic giant branch (AGB) phase of stellar evolution [11]. Therefore, these branchings are crucial for testing the stellar models for this *s*-process site.

The *s*-process path around xenon is sketched in Fig. 1. The *s*-only isotopes ^{128,130}Xe are shielded by their stable Te isobars from the *r* process. Although contributions from the *p* process can not be excluded, these are usually small and are a priori not expected to have a significant impact. As indicated by the thick arrows, the main *s*-process flow is passing through both isotopes. According to the canonical description of the *s*-process, the important quantity $N_s < \sigma >$, the product of *s* abundance and stellar capture cross section, should therefore be equal for both isotopes. This relation may be disturbed, however, by the possibility of two weak branchings at ^{127}Te and ^{128}I which would cause a small part of the reaction flow to bypass ^{128}Xe. In this case the $N_s < \sigma >$-value for ^{128}Xe would be slightly smaller than for ^{130}Xe. Since the abundance ratio of the *s*-only isotopes is accurately known, a possible $N_s < \sigma >$-difference can be detected by an accurate measurement of the cross section ratio.

While the first branching is marginal because the initial population of ground state and isomer are quickly thermalized in the hot stellar photon bath, leading to a strong dominance of the β-decay channel, the second branching at ^{128}I is very interesting. It is only determined by the competition between the two decay modes of ^{128}I, completely independent of the stellar neutron flux. Since the electron capture rate depends on temperature and electron density of the stellar plasma, this branching provides a possibility to test these parameters without an interference from the neutron flux.

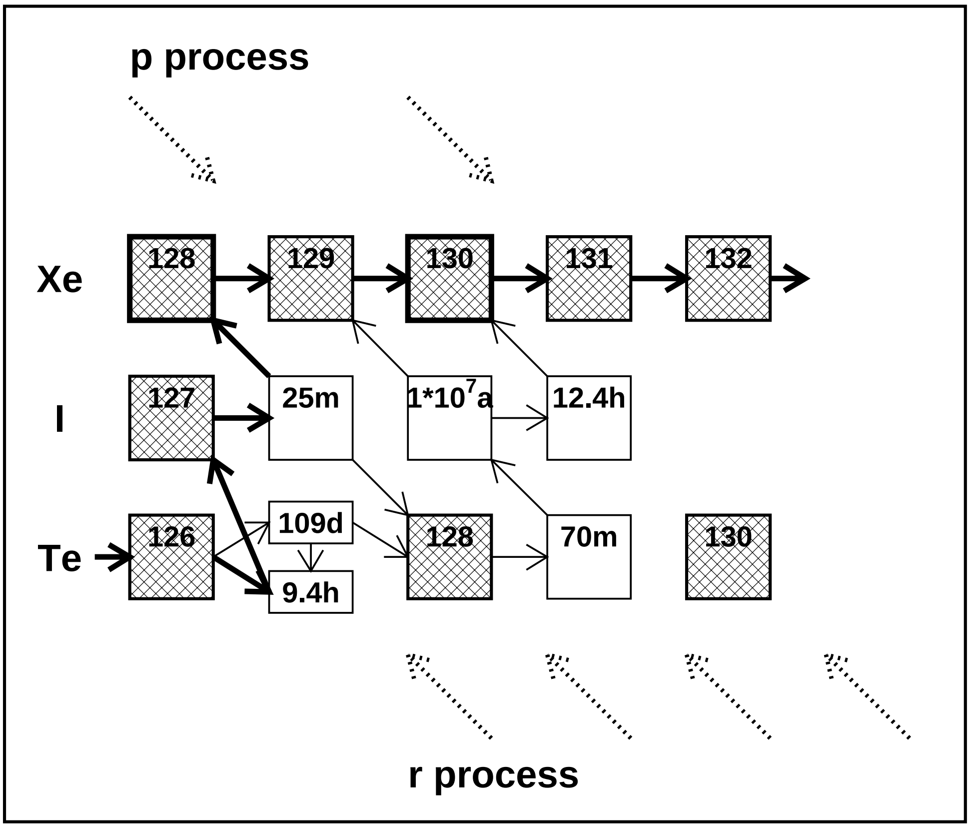

Figure 1: The reaction path of the s process in the region of the xenon isotopes.

Previous (n,γ) data in the keV region were limited partial cross sections of the even xenon isotopes, which were obtained in an activation experiment using a quasi-stellar neutron spectrum for a thermal energy of kT=25 keV [12]. These partial capture cross sections were used to estimate the total stellar cross sections by comparison with the isomeric ratios at thermal neutron energies, resulting in uncertainties of ≈30 %, similar to uncertainties of statistical calculations [2]. This implies that deviations from the local approximation due to a possible branching at ^{128}I, which was expected to be of the order of 10%, could not be distinguished from the unbranched case giving $\mathrm{N}_s < \sigma >$=const. This situation clearly required an accurate measurement of the total neutron capture cross section for the key isotopes ^{128}Xe and ^{130}Xe which would allow to deduce the stellar cross section over the entire range of thermal energies relevant for identifying the branching strength in the framework of a realistic stellar model.

Apart from the branching at ^{128}I, the xenon cross sections are required for determining the solar Xe abundance, which can not be derived in the usual way from the analysis of primitive meteorites or by spectral analyses of the sun [13]. Instead, this quantity has to be defined by means of s-process models, using the fact that the $N_s < \sigma >$ values are almost constant in this mass region. Therefore, the respective values for the Xe isotopes can be interpolated from the isotopes of the neighboring elements. These data in combination with reliable cross sections can hence be used to obtain the solar Xe abundance. In this respect, the unbranched s-only isotope ^{130}Xe is most important.

Furthermore, accurate stellar (n,γ) cross sections are essential for the interpretation that isotopic anomalies found in meteoritic inclusions represent material of pure s-process origin [14].

The measurements are described in Sec. 2. The standard data analysis as well as complementing detailed simulations using the GEANT code are discussed in Secs. 3 and 4, followed by a summary of the results and uncertainties in Secs. 5 and 6. The stellar cross sections obtained from these data are presented in Sec. 7. The astrophysical implications will be addressed in a forthcoming publication.

2 MEASUREMENT

The neutron capture cross sections of the xenon isotopes 128 to 130 have been measured in the energy range from 3 to 225 keV using gold as a standard. Since the experimental method has been published in detail [1, 7, 8, 15], only a general description is given here, complemented with the specific features of the present measurement.

Neutrons were produced via the $^7\mathrm{Li}(p,n)^7\mathrm{Be}$ reaction by bombarding metallic Li targets with the pulsed proton beam of the Karlsruhe 3.75 MV Van de Graaff accelerator. The neutron energy was determined by time of flight (TOF), the samples being located at a flight path of 79 cm. The relevant parameters of the accelerator were a pulse width of <1 ns, a repetition rate of 250 kHz, and an average beam current of 2.2 μA. In different runs, the proton energies were adjusted 30 and 100 keV above the threshold of the $^7\mathrm{Li}(p,n)^7\mathrm{Be}$ reaction at 1.881 MeV. In this way, continuous neutron spectra in the proper energy range for s–process studies were obtained, ranging from 3 to 100 keV, and 3 to 225 keV, respectively. The lower maximum neutron energy offers a significantly better signal-to-background ratio at lower energies. The neutron beam was collimated to a nominal diameter of 12 mm at the sample position.

Capture events were registered with the Karlsruhe 4π Barium Fluoride Detector via the prompt capture γ–ray cascades. This detector consists of 42 hexagonal and pentagonal crystals forming a spherical shell of BaF_2 with 10 cm inner radius and 15 cm thickness. It is characterized by a resolution in γ–ray energy of 7% at 2.5 MeV, a time resolution of 500 ps, and a peak efficiency of 90% at 1 MeV. The 1.6 MeV threshold in γ–ray energy used in the present experiment corresponds to an efficiency for capture events of more than 95% for all investigated isotopes. A comprehensive description of this detector can be found in Ref. [15].

2.1 Samples

The main experimental problem was the preparation of appropriate samples. In a recent experiment on krypton isotopes [16] the situation for experiments using electron linear accelerators can be illustrated as a typical example. Samples of ∼18g were used for each isotope, enclosed in aluminum spheres with 8 cm diameter and 1 mm thick walls. Accordingly, the total aluminum mass of 56 g exceeded the weight of the investigated isotopes by about a factor of three.

Due to the efficiency of the Karlsruhe $4\pi BaF_2$ detector for capture events of nearly 100% as well as the high neutron flux which is available at the short flight path, much smaller samples could be used in the present experiment. These consisted of ≈0.5g highly enriched xenon gas enclosed in titanium spheres of 10 mm diameter and a wall thickness of 0.2 mm. The schematic sketch shown in Fig.2 illustrates also the very thin filling port and the steel valve, which was outside the neutron beam. This valve is operated by pressing a polished steel sphere onto a konical fit by means of a headless screw. During the filling procedure a small spring is lifting the sphere from the fit.

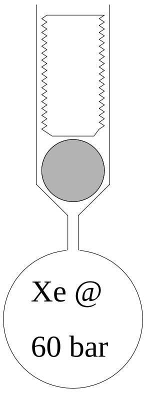

Figure 2: Schematic sketch of the sample can.

The Ti spheres were made by rolling the available 0.5 mm thick metal sheets to a nominal thickness of 0.2 mm, which were used to form hemispheres. After the filling port was connected the hemispheres were put together by electron beam welding. While the total mass of the spheres is about 3 g, the spherical part inside the neutron beam was only 300 mg.

After manufacturing, all cans were marked with an identification number. First tests with Ar gas confirmed that these cans could be safely operated up to pressures of 100 bar, corresponding to 700 mg xenon. Accordingly, these cans allowed for a significantly better signal to background ratio compared to the experiment mentioned before.

In total, 2 g of ^{128}Xe, 5.7 g of ^{129}Xe and 4g of ^{130}Xe were available. In order to check for systematic uncertainties two samples of $\approx$500 mg were prepared for each isotope and the six samples were measured in the same experiment.

Filling of the samples occurred in two steps, by transfering the enriched xeneon gas first into an intermediate storage volume consisting of an 0.28 l stailess steel bottle which was connected to the Ti spheres by very thin tubes. After evacuating the whole system, a certain amount of gas was frozen into the intermediate volume. Then, the stainless steel bottle was brought to room temperature and the pressure in the intermediate volume was determined. In the next step the valve to the sample was opened and the xenon mass frozen into the sphere was controlled via the pressure decrease in the storage volume. Finally, the valve of the titanium sphere was closed and the remaining gas was frozen back into the stainless steel bottle.

The Xe sample mass was determined from the difference in weight before and after filling procedure. The weight of the samples was monitored for several days before the start of the measurements to ensure that there were no Xe losses. The weight of the xenon samples was also controlled after each experimental run. All turned out to be reliably tight, the only exception being sample 8. After the experiment the enriched gas was refilled into the bottles for permanent storage.

The Ti spheres with the six xenon samples were mounted on the ladder of a sample changer, which held also a gold sample for measuring the neutron flux. The gold sample consisted three 0.125 mm thick disks of 8, 10, and 8 mm diameter enclosed in an identical Ti sphere. Two additional Ti spheres were used for background measurements, an evacuated, empty sphere for determining the ambient component, and one filled with a graphite ball of 10 mm diameter for determining the background due to scattered neutrons.

The relevant sample parameters are compiled in Table 1, including the identification number of the respective Ti spheres and the weight of the xenon content at different times during the experiment. In general, the sample mass was fairly constant over the entire period of nearly 9 months, the small changes being consistent with the 0.1 mg uncertainty of the balance. A significant loss was observed for sample 8, however. Since the large cross section of the ^{129}Xe allowed to achieve sufficient counting statistics from the second ^{129}Xe sample, the leaky sphere was removed after the first run. In view of the comparably small cross section of ^{130}Xe, sample 13 was replaced after the first run as indicated in the last column of Table 1. The isotopic composition of the xenon samples is given in Table 2.

2.2 Experimental runs

The experiment was divided into three runs, two using the conventional data acquisition technique with the detector operated as a calorimeter. In the third run an analog-to-digital converter (ADC) system coupled to the detector for analyzing the signals from all modules individually. In this way, the full spectroscopic information recorded by the detector can be recovered.

The measured spectra of all samples were normalized to equal neutron flux by means of a ^{6}Li–glass monitor located close to the neutron target.

The collimated neutron beam at the sample position was 12 mm in diameter. Consequently, only the titanium spheres with a total mass of $\approx$0.3 g were exposed to the beam. Since the cross section of titanium is much smaller compared to the investigated xenon isotopes, the corresponding background had no significant impact on the experimental sensitivity.

The samples were moved cyclically into the measuring position by a computer controlled sample changer. The data acquisition time per sample of about 10 min was determined by the integrated proton beam current on target, a complete cycle lasting about 1.5 h. From each event, a 64 bit word was recorded on DAT tape containing the sum energy and TOF information together with 42 bits identifying those detector modules that contributed.

The relevant parameters of the three runs corresponding to neutron spectra with different maximum energies are listed in Table 3. Instead of the leaky ^{129}Xe sample, which was removed after the first run, data were taken from an empty position in the sample changer in all further runs.

Table 1: SAMPLE CHARACTERISTICS

Sample	Number	Weight[1] (mg)	Weight[2] (mg)	Weight[3] (mg)	Weight[4] (mg)	Loss (mg)	Sphere[5] (g)	B_n[6] (MeV)	Runs
Date:		24.09.99	19.10.99	17.04.00	14.06.00				
^{129}Xe	7	499.25	499.18	499.19	498.05	0.3	3.0289	9.2550	I,II,III
^{129}Xe	8	537.03	528.27		528.13	8.9	3.0194	9.2550	I
^{128}Xe	10	367.37	366.97	365.41	365.66	1.71	3.0147	6.9078	I,II,III
^{128}Xe	11	478.42	478.37	478.30	478.28	0.14	3.0227	6.9078	I,II,III
^{130}Xe	12	673.69	673.55	673.46	674.30	-0.61	3.0290	6.125	I,II,III
^{130}Xe	13	471.44	470.05	470.03	470.96	0.48	3.0169	6.125	I
^{130}Xe	14	637.86	637.82	637.70	638.23	-0.37	3.0136	6.125	II,III
^{197}Au		441.0					3.1434	6.512	I,II,III
Graphite		157.7					3.1363		I,II,III
Empty	4						3.0515		I,II,III

[1] Weight of Xe gas after filling.
[2] Weight of Xe gas at start of measurements.
[3] Weight of Xe gas at end of measurements.
[4] Weight of Xe gas before refilling into gas bottles.
[5] Weight of the evacuated sphere.
[6] Binding energy of the captured neutron.

Table 2: ISOTOPIC COMPOSITION (%)

Sample	Isotope		
	^{128}Xe	^{129}Xe	^{130}Xe
^{128}Xe	99.6	0.4	0.0
^{129}Xe	0.04	99.95	0.01
^{130}Xe	0.0	0.3	99.7

Table 3: PARAMETERS OF THE INDIVIDUAL RUNS

Run	Flight Path (mm)	TOF Scale (ns/ch)	Number of Cycles	Maximum Neutron Energy (keV)	Measuring Time (d)	Mode of Operation	Average Beam Current (μA)	Threshold in Sum Energy (MeV)
I	788.0	0.7604	289	100	20.7	Calorimeter	1.7	1.7
II	787.8	0.7603	338	200	22.8	Calorimeter	1.8	1.6
III	788.1	0.7087	322	100	18.1	ADC	1.7	1.6

3 DATA ANALYSIS

Due to the sperical geometry of the xenon samples it was not possible in the present experiment do derive information on the total cross section from the spectra measured with a ^{6}Li neutron monitor at a flight path of 260 cm.

The data of all samples were evaluated separately. In this way, two sets of cross sections were derived for each xenon isotope together with the respective uncertainties. Since the samples differed significantly in weight, the consistency of the resulting cross sections confirmed that the xenon gas was not contaminated by impurities during the filling procedure. The final cross sections were then obtained as the weighted average.

The analysis of the capture cross section was carried out in the same way as described previously [1, 7, 8]. All events were sorted into two–dimensional spectra containing 128 sum energy versus 2048 TOF channels according to various event multiplicities (evaluation 1). In evaluation 2, this procedure was repeated by rejecting those events, where only neighboring detector modules contributed to the sum energy signal. With this option, background from the natural radioactivity of the BaF$_2$ crystals and from scattered neutrons can be reduced. For all samples, the resulting spectra were normalized to equal neutron flux using the count rate of the ^{6}Li glass monitor close to the neutron target. The corresponding normalization factors are below 0.5% for all runs. The treatment of the two-dimensional spectra from the data recorded with the ADC system is slightly more complicated and was performed as described in Ref. [8].

In the next step of data analysis, sample-independent backgrounds were removed by subtracting spectra measured with the empty Ti sphere. This was justified since the weight of the spheres (Table 1) was almost identical for all samples. A remaining constant background was determined at very long flight times, where no time-correlated events are expected. The resulting two-dimensional spectra for events with multiplicity >2 measured in run I are shown for all investigated isotopes in the middle part of Figs. 3, and 4.

At this point, the spectra contain only events correlated with the sample. The next correction to be made is for isotopic impurities (see Ref.[8] for details). The respective coefficients are compiled in Table 4. Due to the high enrichment of 99% this correction is extremely small for all samples and could have been neglected in the present experiment. The matrix for isotopic correction had to be calculated for each run separately because more than one sample had been used per isotope and because some samples were exchanged between runs. For example, the matrix of Table 4 was used to analyse the spectra measured in run I with samples 8, 11, and 12 (see Table 1), while a similar matrix was required for the analysis of samples 7, 10, and 13. The coefficients are very small and can be positive or negative as a consequence of the isotopic composition. In the first line of Table 4 the spectrum of ^{128}Xe is corrected for the ^{129}Xe contamination by subtracting the scaled ^{129}Xe spectrum. This implies, however, that the respective ^{130}Xe contribution is overcorrected. Therefore, this part has to be added, leading to a positive coefficient for ^{130}Xe.

Following the correction for isotopic impurities, the background due to capture of sample scattered neutrons was removed from the spectra by means of the data measured with the graphite scattering sample. The binding energy of the even xenon isotopes is low enough, that the correction can be normalized at the pronounced peak in the sum-energy spectra at 9.1 MeV due to capture in the odd barium isotopes ^{133}Ba and ^{135}Ba (see Figs. 5,and 6). In case of ^{129}Xe, which has a binding energy of 9.2 MeV, this feature is hidden under the full energy peak. Instead, the normalization has to rely on the peak at 6.8 MeV due to captures in the even barium isotopes, which sits on the tail of the true capture events. The determination of this correction is described in Ref. [7] for example.

The present setup has the advantage that this correction can be determined as a function of neutron energy. In the interval from 50 to 100 keV illustrated in Figure 5 the scattering background below the actual capture peak is comparably small since the graphite spectrum has to be normalized by a factor of $\approx$0.2 in order to match the measured spectrum around 9.1 MeV. This situation is slightly worse in the interval from 30 to 60 keV shown in Fig. 6 where the normalized intensity of the graphite spectrum is shown by the hatched area.

After this last correction, the spectra contain only the capture events of the investigated isotopes (bottom spectra in Figs. 3, 4) The backgrounds due to capture of scattered neutrons are shown explicitely in Fig. 7, and the corresponding signal/background ratios are listed in Table 5 for different neutron energies.

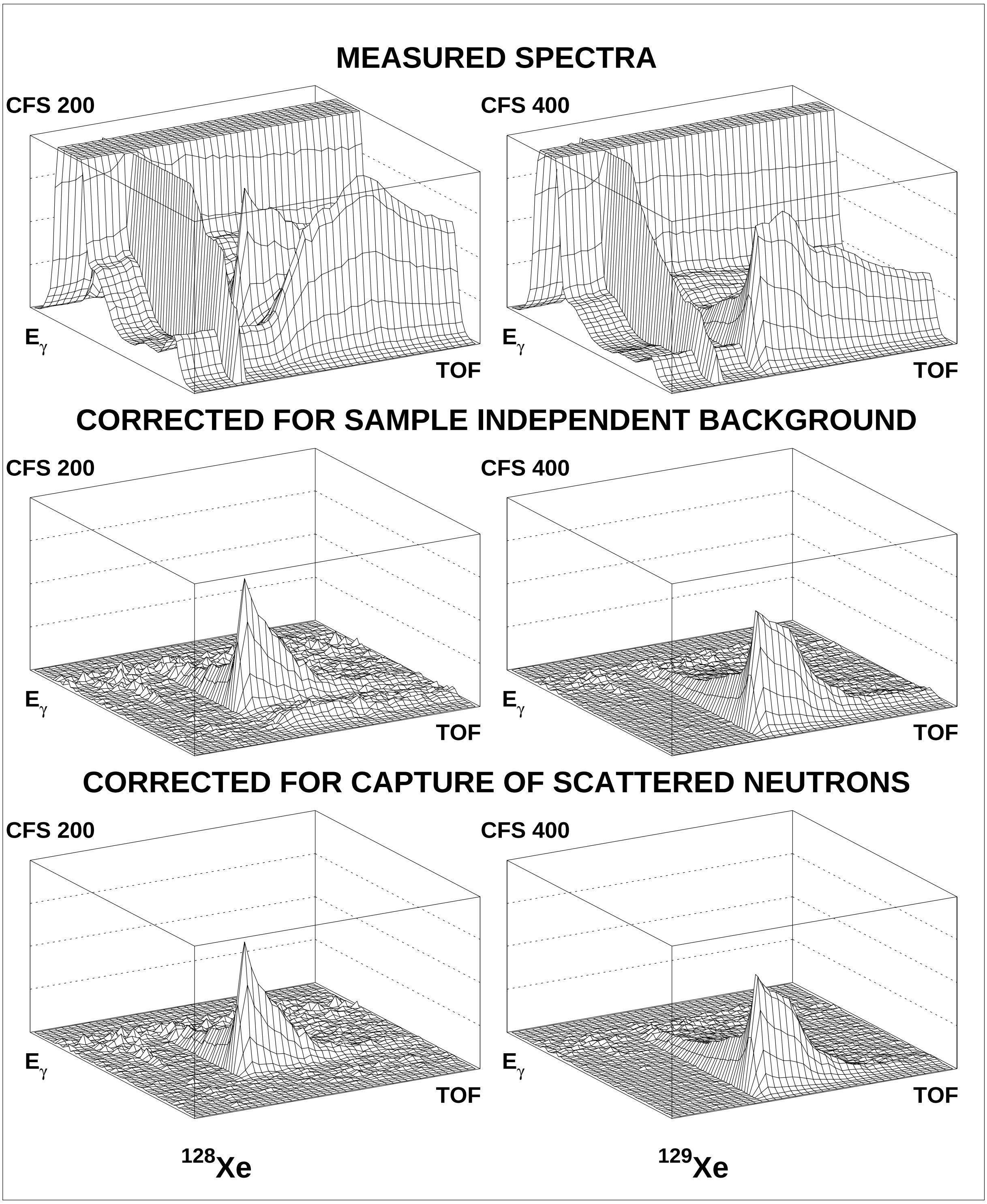

Figure 3: The different steps of background subtraction in the two–dimensional sum energy × TOF spectra. The data are shown for ^{128}Xe and ^{129}Xe measured in run I with 100 keV maximum neutron energy. Only events with multiplicity >2 are shown. (The original resolution of 128 × 2048 channels was compressed into 64 × 64 channels for better readability.)

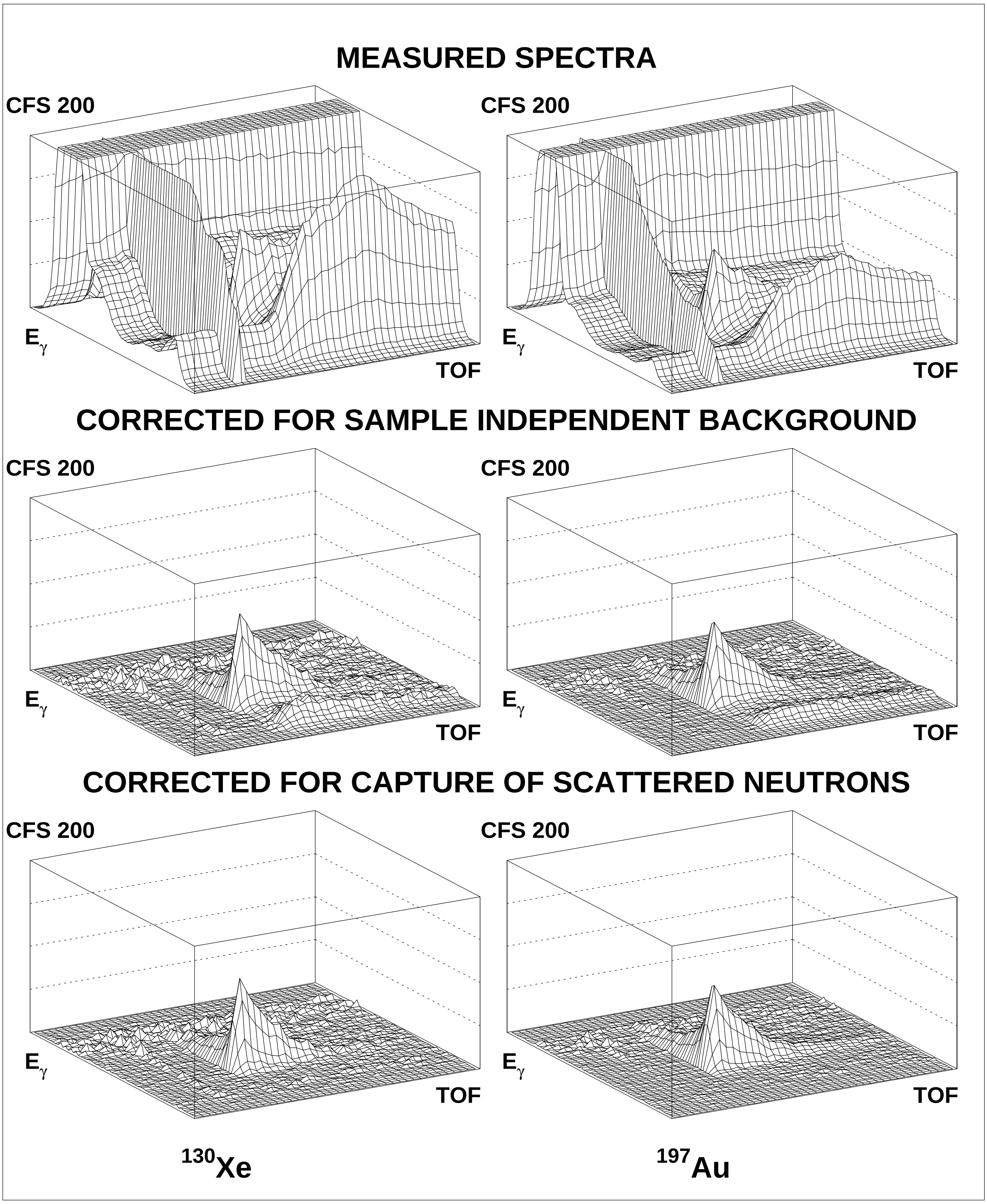
MEASURED SPECTRA

CORRECTED FOR SAMPLE INDEPENDENT BACKGROUND

CORRECTED FOR CAPTURE OF SCATTERED NEUTRONS

Figure 4: As Fig. 3 but for the ^{130}Xe and ^{197}Au samples.

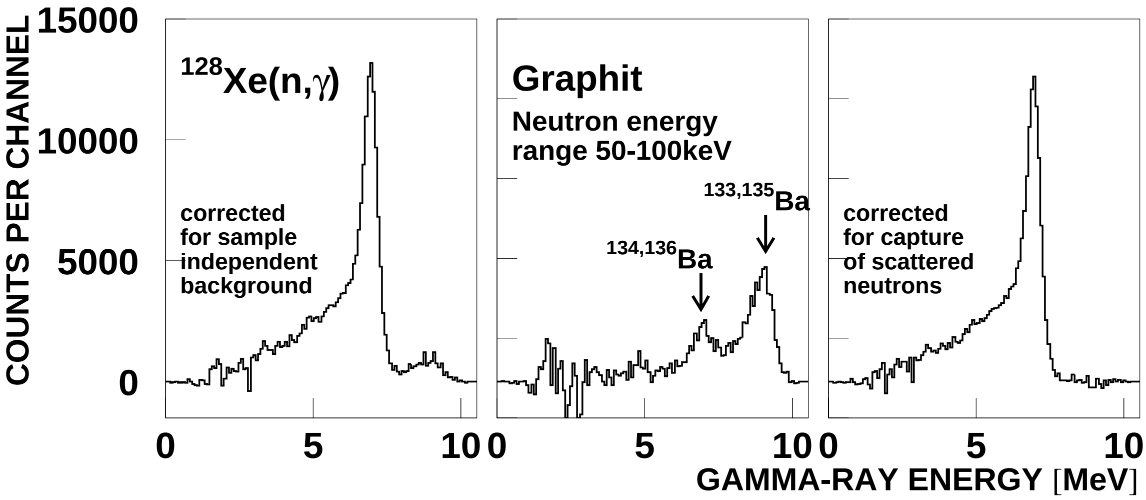

Figure 5: Background subtraction due to capture of scattered neutron in the neutron energy interval from 50 - 100 keV.

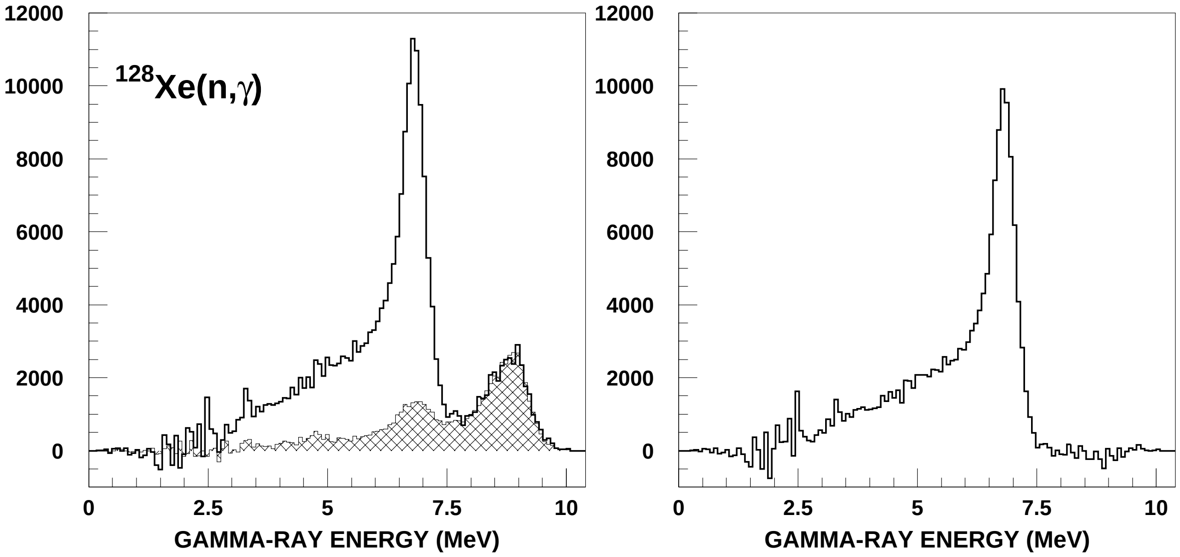

Figure 6: Background subtraction due to capture of scattered neutron in the neutron energy range from 30 to 60 keV. The measured spectrum is shown in the left part together with the normalized graphite spectrum (hatched area). The normalization factor is calculated to match the intensity around 9.2 MeV. The corrected spectrum is shown in the right part of the figure.

Table 4: MATRIX FOR ISOTOPIC CORRECTIONS (%)

Corrected spectrum	Measured spectrum			Corrected sample thickness[a]
	^{128}Xe	^{129}Xe	^{130}Xe	10^{-3} at/barn)
^{128}Xe	100	−0.363	+0.000028	2.8542
^{129}Xe	+0.044	100	−0.0079	3.1386
^{130}Xe	+0.000017	−0.3797	100	3.9606

[a] nominal thickness calculated using a sample diameter of 10 mm.

Table 5: SIGNAL/BACKGROUND RATIO DUE TO SCATTERED NEUTRONS

Sample	$\sigma_{tot}/\sigma_{n,\gamma}$	Maximum neutron energy	Signal/Background ratio[a]		
	E$_n$=30 keV	(keV)	E$_n$=30 keV	E$_n$=20 keV	E$_n$=10 keV
^{128}Xe	30	100	6.8	4.4	2.4
^{129}Xe	11		9.3	4.7	2.8
^{130}Xe	61		4.9	2.6	2.1
^{197}Au	24		7.8	3.9	2.9
^{128}Xe		200	4.6	3.6	2.3
^{129}Xe			6.6	3.7	2.6
^{130}Xe			3.3	2.3	2.3
^{197}Au			6.0	2.9	2.3

[a](detected capture events + neutron scattering background)/(neutron scattering background)

After subtraction of the scattering background the cross section shape versus neutron energy was determined from the TOF spectra of Fig. 7. These spectra are calculated by integrating the two-dimensional spectra in a region around the full energy peak. According to the different background conditions for events with different multiplicities, a broader interval was accepted for multiplicity ≥ 5 and increasingly smaller intervals at lower multiplicities (see Fig. 9). For normalization, the two-dimensional data were projected onto the sum energy axis using the TOF region with optimum signal/background ratio as indicated in Fig. 7 by vertical lines. The resulting pulse height spectra are shown in Fig. 8 for events with multiplicity >2. The threshold in sum energy is 1.6 MeV.

The sum energy spectra of all isotopes are shown in Fig. 9 for different measured multiplicities. These correspond to the number of detector modules contributing per event, and are slightly larger than the true multiplicities because of cross talking between modules. In the even xenon isotopes ≈40% of the capture events are observed with multiplicities ≥5, while the respective fraction in the odd isotope is about 65%. The arrows in Fig. 9 indicate the range of sum energy channels that were integrated to obtain the TOF spectra of Fig. 7.

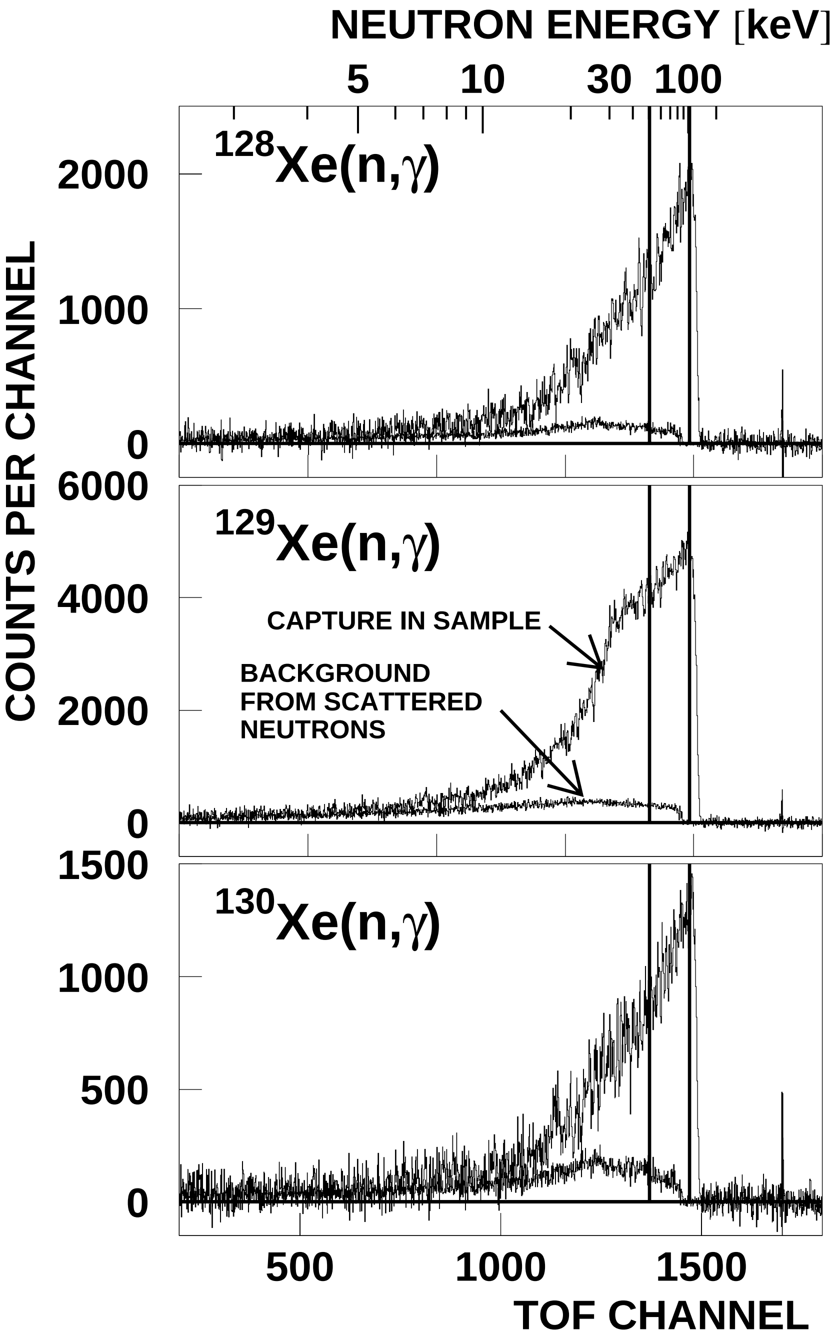

Figure 7: TOF spectra measured with the xenon samples in run I (100 keV maximum neutron energy). The background due to sample scattered neutrons is shown separately. The region used for absolute normalization of the cross section is indicated by vertical lines.

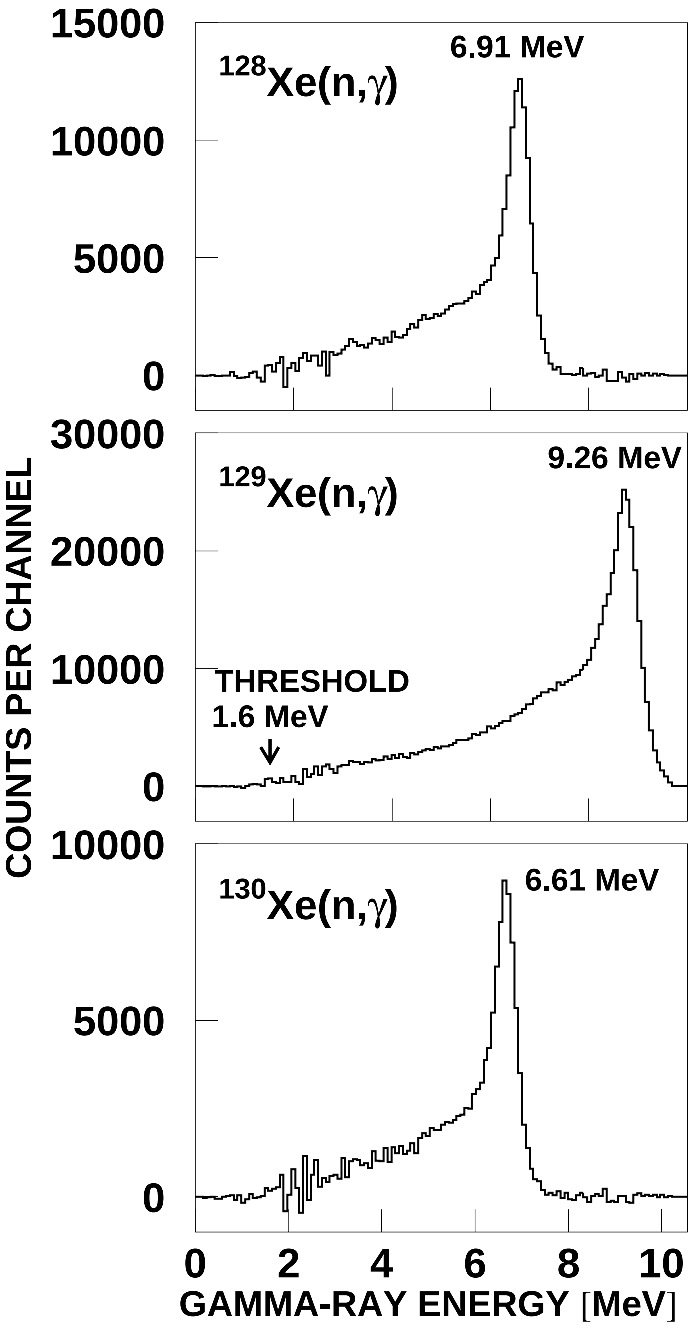

Figure 8: Sum energy spectra of all isotopes measured in run III containing events with multiplicity >2. These spectra were obtained by projection of the two-dimensional spectra in the TOF region below the maximum neutron energy as indicated by vertical lines in Fig. 7.

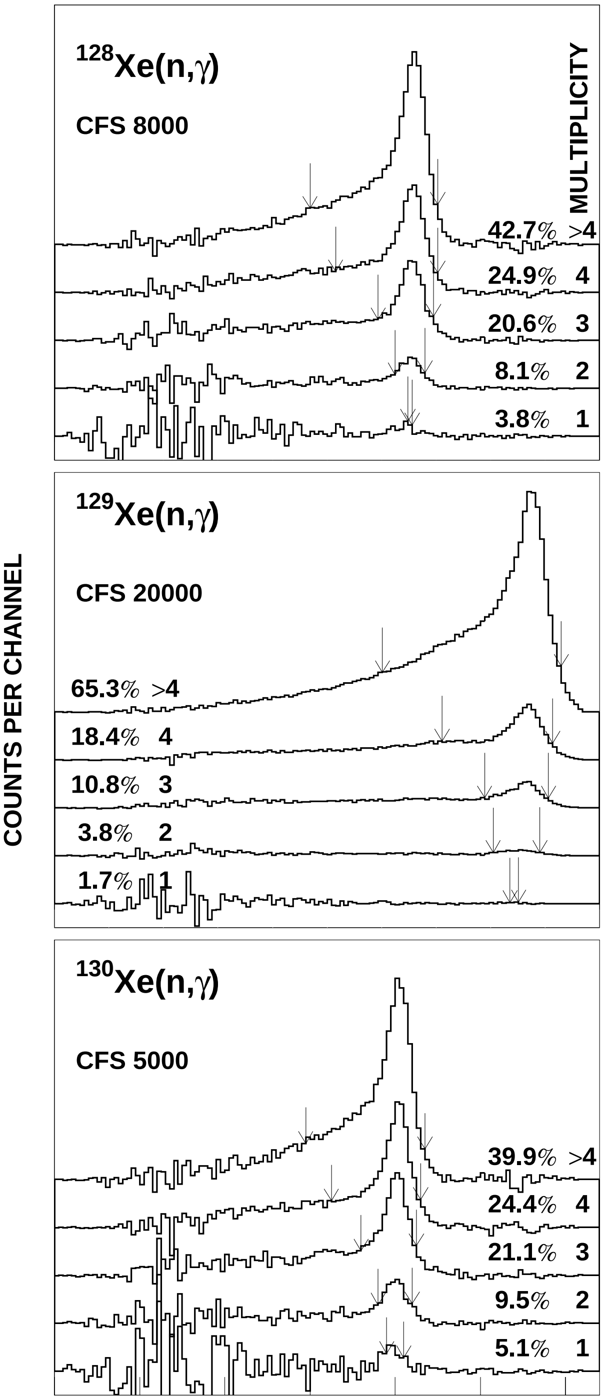

Figure 9: Sum energy spectra of all isotopes as a function of multiplicity. The regions integrated to determine the cross section shape (see TOF spectra of Fig. 7) are indicated by arrows.

The cross section ratio of isotope X relative to the gold standard is given by

$$\frac{\sigma_i(X)}{\sigma_i(Au)} = \frac{Z_i(X)}{Z_i(Au)} \frac{\Sigma Z(Au)}{\Sigma Z(X)} \frac{\Sigma E(X)}{\Sigma E(Au)} \frac{m(Au)}{m(X)} F_1 F_2 \tag{1}$$

In this expression, Z_i is the count rate of channel i in the TOF spectrum, ΣZ is the TOF rate integrated over the interval used for normalization (vertical lines in Fig. 7), ΣE is the total count rate in the sum energy spectra for all multiplicities in this TOF interval. The respective sum energy spectra are shown in Fig. 9. For all multiplicities these spectra were integrated from the threshold at 1.7 MeV well beyond the binding energy, the resulting sums, ΣE, being used in Eq. (1). A detailed description of this procedure is given in Ref.[17]. The quantity m denotes the sample thickness in atoms/b. The fraction of capture events f below the experimental threshold in sum energy is accounted for by the correction $F_1 = [100 - f(Au)]/[100 - f(X)]$, where X refers to the respective xenon sample (Table 6). F_2 is the ratio of the multiple scattering and self-shielding corrections.

The fraction of unobserved capture events, f, and the correction factor F_1 were calculated as described in Ref. [1] and are listed in Table 6. Apart from the detector efficiency for monoenergetic γ-rays in the energy range up to 10 MeV, the neutron capture cascades and their relative contributions to the total capture cross section represent the relevant input for this calculation. As described in Ref. [18] this information was derived directly from the experimental data recorded with the ADC system. For this procedure, only events close to the sum energy peak (see Fig. 8) were selected, which contained the full capture γ-ray cascade. This ensemble was further reduced by restricting the analysis to the TOF region with optimum signal/background ratio (vertical lines in Fig. 7). As in all previous experiments with the 4π BaF_2 detector, F_1 was found to depend linearly on the binding energy of the captured neutrons.

The capture γ-ray spectra deduced from the data taken with the ADC system are shown in Fig. 10 in energy bins of 500 keV The spectra of the even target isotopes show a significant hard component, evidence for strong primary transitions to low-lying states.

The correction for neutron multiple scattering and self-shielding was calculated with the SESH code [19]. Since SESH is limited to cylindrical samples, the spherical geometry was approximated by a cylinder of equal volume, 9 mm in diameter and 8.2 mm long. Apart from the pairing energies [20], most of the input parameters for these calculations were taken from Ref. [21]. These data required some minor modifications for reproducing the measured capture cross sections. The final values are listed in Table 7 together with the calculated total cross sections. The resulting correction factors, MS(X) and F_2, are compiled in Tables 8 and 9.

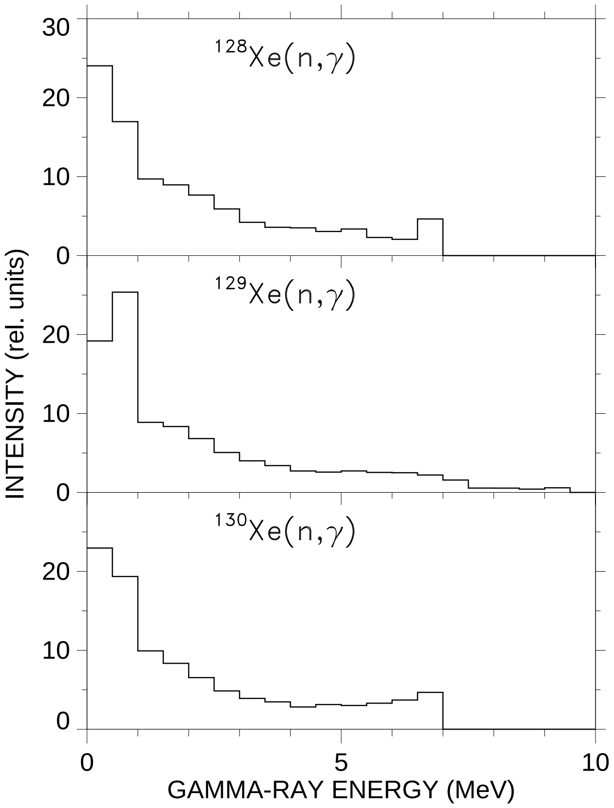

Figure 10: Capture γ-ray spectra derived from the capture cascades recorded with the ADC system. (The full resolution of 2048 channels is compressed into bins of 500 keV.)

Table 6: FRACTION OF UNDETECTED CAPTURE EVENTS, f (%), AND THE RELATE CORRECTION FACTORS F_1.[a]

	Threshold in Sum Energy (MeV)			
	1.5	1.6	1.7	2.0
f(Au)	4.92			6.87
f(^{128}Xe)	3.44			4.94
f(^{129}Xe)	1.19			1.83
f(^{130}Xe)	4.39			5.98
F_1(^{128}Xe/Au)	0.985	0.984	0.983	0.980
F_1(^{129}Xe/Au)	0.962	0.960	0.957	0.949
F_1(^{130}Xe/Au)	0.994	0.994	0.993	0.991

[a] derived from capture cascades measured with the ADC system

Table 7: PARAMETERS FOR THE CALCULATION OF NEUTRON SELF–SHIELDING AND MULTIPLE SCATTERING CORRECTIONS

Parameter		^{128}Xe	^{129}Xe	^{130}Xe	^{197}Au
Nucleon Number		128	129	130	197
Binding Energy (MeV)		6.908	9.255	6.612	6.513
Pairing Energy (MeV)		1.120	2.32	1.120	0.0
Effective Temperature (K)		293	293	293	293
Nuclear Spin		0	0.5	0	1.5
Average Radiation	s	0.100	0.250	0.080	0.128
Width (eV)	p	0.040	0.080	0.040	0.048
	d	0.040	0.080	0.040	0.048
Average Level	s	105.	45.	250.	16.5
Spacing (eV)	p[a]	35.0	20.	83.3	8.25
	d[a]	21.0	12.	50.0	5.28
Strength Function	S_0	1.2	2.0	1.2	2.0
(10^{-4})	S_1	2.0	2.0	2.0	0.4
	S_2	1.0	1.0	1.0	0.7
Nuclear Radius	s	6.00	5.50	6.00	9.5
(fm)	p	6.00	5.50	6.00	9.5
	d	6.00	5.50	6.00	9.5
		Calculated total cross sections			
3 keV		13.8	19.2	13.8	26.1
5 keV		11.9	15.8	11.9	22.6
10 keV		9.9	12.4	9.9	18.9
20 keV		8.6	10.1	8.6	16.1
40 keV		7.7	8.5	7.7	13.8
80 keV		7.1	7.4	7.1	11.7
160 keV		6.7	6.7	6.7	9.6
320 keV		6.4	6.1	6.4	7.6

[a] Calculated with SESH [19]

Table 8: CORRECTION FACTORS FOR NEUTRON SELF–SHIELDING AND MULTIPLE SCATTERING, MS

Energy Bin	MS							
(keV)	^{197}Au	^{128}Xe		^{129}Xe		^{130}Xe		
Sample Number		10	11	7	8	12	13	14
3 – 5	0.998	0.914	0.893	0.899	0.894	0.848	0.884	0.855
5 – 7.5	1.013	0.946	0.933	0.935	0.932	0.898	0.924	0.903
7.5 – 10	1.022	0.962	0.951	0.955	0.952	0.925	0.945	0.929
10 – 12.5	1.027	0.970	0.962	0.967	0.965	0.942	0.958	0.944
12.5 –15	1.029	0.974	0.968	0.973	0.971	0.950	0.963	0.952

Table 8 (continued)

15 – 20	1.029	0.979	0.974	0.980	0.979	0.959	0.971	0.961
20 – 25	1.029	0.984	0.979	0.984	0.984	0.967	0.976	0.969
25 – 30	1.029	0.986	0.982	0.987	0.987	0.971	0.980	0.973
30 – 40	1.028	0.988	0.985	0.991	0.991	0.976	0.984	0.978
40 – 50	1.027	0.991	0.989	0.992	0.992	0.980	0.986	0.981
50 – 60	1.026	0.992	0.990	0.993	0.993	0.981	0.988	0.983
60 – 80	1.025	0.993	0.991	0.994	0.994	0.984	0.989	0.985
80 – 100	1.024	0.994	0.992	0.995	0.995	0.985	0.990	0.986
100 – 120	1.023	0.995	0.992	0.996	0.996	0.986	0.990	0.987
120 – 150	1.022	0.995	0.993	0.997	0.997	0.987	0.991	0.987
150 – 175	1.021	0.995	0.993	0.997	0.997	0.987	0.991	0.987
175 – 200	1.021	0.995	0.993	0.997	0.997	0.989	0.991	0.989
200 – 225	1.020	0.995	0.994	0.997	0.997	0.990	0.992	0.990
Uncertainty (%)	0.3	0.2	0.2	0.1	0.1	0.3	0.3	0.3

Table 9: CORRECTION FACTORS FOR THE CROSS SECTION RATIOS, $F_2 = MS(Au)/MS(X)$

Energy Bin	F_2						
(keV)	^{128}Xe/Au		^{129}Xe/Au		^{130}Xe/Au		
Sample Number	10	11	7	8	12	13	14
3 – 5	1.092	1.118	1.110	1.116	1.177	1.129	1.167
5 – 7.5	1.071	1.086	1.083	1.087	1.128	1.096	1.122
7.5– 10	1.062	1.075	1.070	1.074	1.105	1.082	1.100
10 – 12.5	1.059	1.068	1.062	1.064	1.090	1.072	1.088
12.5 – 15	1.056	1.063	1.058	1.060	1.083	1.069	1.081
15 – 20	1.051	1.056	1.050	1.051	1.073	1.060	1.071
20 – 25	1.046	1.051	1.046	1.046	1.064	1.054	1.062
25 – 30	1.044	1.048	1.043	1.043	1.060	1.050	1.058
30 – 40	1.041	1.044	1.037	1.037	1.053	1.045	1.051
40 – 50	1.036	1.038	1.035	1.035	1.048	1.042	1.047
50 – 60	1.034	1.036	1.033	1.033	1.046	1.038	1.044
60 – 80	1.032	1.034	1.031	1.031	1.042	1.036	1.041
80 – 100	1.030	1.032	1.029	1.029	1.040	1.034	1.039
100 – 120	1.028	1.031	1.027	1.027	1.038	1.033	1.036
120 – 150	1.027	1.029	1.025	1.025	1.035	1.031	1.035
150 – 175	1.026	1.028	1.024	1.024	1.034	1.030	1.034
175 – 200	1.026	1.028	1.024	1.024	1.032	1.030	1.032
200 – 225	1.025	1.026	1.023	1.023	1.030	1.028	1.030
Uncertainty (%)	0.4	0.4	0.3	0.3	0.4	0.4	0.4

4 GEANT SIMULATIONS

Detailed simulations with the GEANT code [6] have recently led to a significantly improved understanding of the performance of the Karlsruhe 4π BaF_2 detector [5]. In this approach the advantage of GEANT in modeling complex detector geometries was complemented by an effort to improve the database for low energy neutrons and by implementing the most recent evaluations for the relevant neutron and gamma cross sections.

The geometry of the Karlsruhe 4π BaF_2 detector was accurately defined for all 41 modules including the supporting structures as well as rather fine details such as reflector sheets and photomultipliers The efficiency for γ-rays originating from a sample in the center of the detector was then calculated including γ-ray self absorption corrections in the sample and in the Ti spheres. In this context it was important that also the effect of internal conversion could be considered. Since the conversion electrons are easily absorbed in the sample or the canning of the barium fluoride crystals they do not contribute to the scintillation signal in the barium fluoride crystals. For the first time, this effect could be investigated quantitatively.

In this way, the γ-response for single modules as well as the probability for cross talking between modules could be reliably evaluated The energy resolution of individual crystals was considered by adopting experimentally determined information obtained in measurements with the ADC system.

True events were simulated by means of capture γ-ray cascades, which were calculated for the investigated xenon isotopes and for gold by using CASINO [22], an extension of the Monte Carlo code DICEBOX [23] for the keV neutron energy range. This approach allows to treat the probability for the emission of conversion electrons properly. For each set of input parameters about 10000 neutron capture cascades were calculated, with a flag on each transition to distinguish γ-rays and conversion electrons.

With these calculated cascades the response of the $4\pi BaF_2$ detector was determined in the GEANT simulations by following γ-rays and electrons from their points of origin, which were isotropically distributed over the volume of the sample. The energy deposit in the individual detector modules was considered down to the experimental threshold of $\approx$50 keV. Since each capture cascade was treated separately, the sum energy spectra could be determined in dependence of the event multiplicity defined in Sec.3, which corresponds to the number of modules with an energy deposit above the 50 keV threshold. The total recorded cascade energy (sum energy) was then stored in the respective multiplicity spectrum. Even multiplicities between 1 and 15 were found in the simulations, in close correspondence to the experimental xenon spectra as shown in Figs. 11, 12,and 13. The simulated spectra are indicated by the hatched area, while the experimental results are shown as histograms. The spectrum in the upper left corner of each figure corresponds to the total sum of all multiplicities. It is important to note that the integrated number of events in these sum spectra are the only normalization factors involved. The simulated spectra for the various multiplicities were not adjusted to the experimental data but simply scaled by using the same normalized factor, illustrating the remarkable quality of the calculated capture cascades as well as of the simulations.

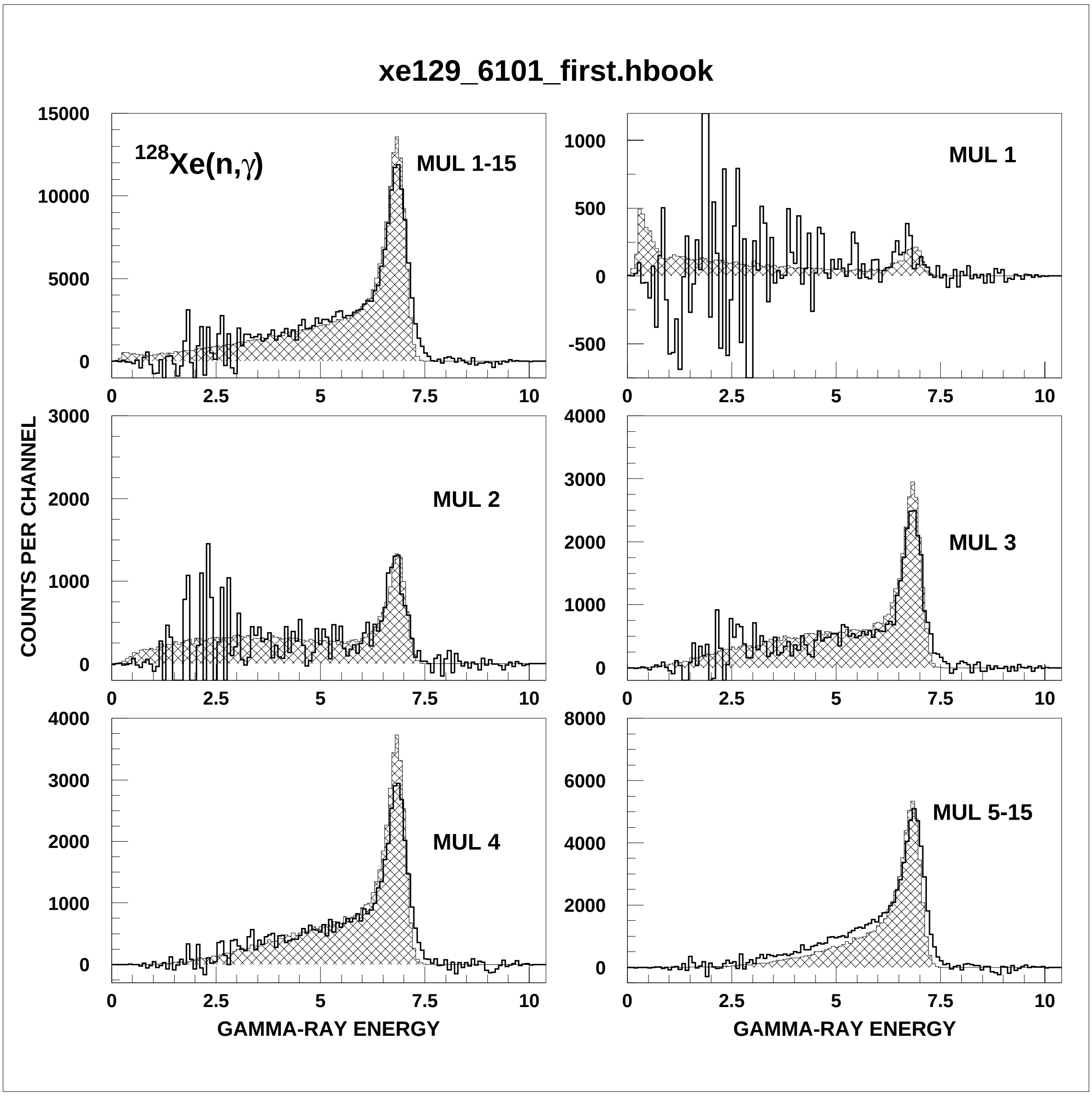

Figure 11: Simulated sum energy spectra for capture in ^{128}Xe for different multiplicities (hatched) compared to the experimental spectra shown in Fig. 9 (histogram).

This is also obvious from the surprisingly good agreement in the shape of the measured and simulated spectra. Not only the full energy peak at the binding energy of the captured neutron but also the tail towards lower energies is correctly described. For all three Xe isotopes the experimental spectra are well reproduced even for multiplicities 1 and 2 where the subtraction of a large background component gives rise to strong fluctuations. If the capture cascades were calculated with different sets of input parameters, the agreement between simulation and experiment was significantly worse in certain cases. In principle, this can be used for testing the physics of the capture process.

The corresponding comparison for the gold sample (Fig 14) exhibits similarly good agreement between experiment and simulation as for the Xe isotopes, especially the to-

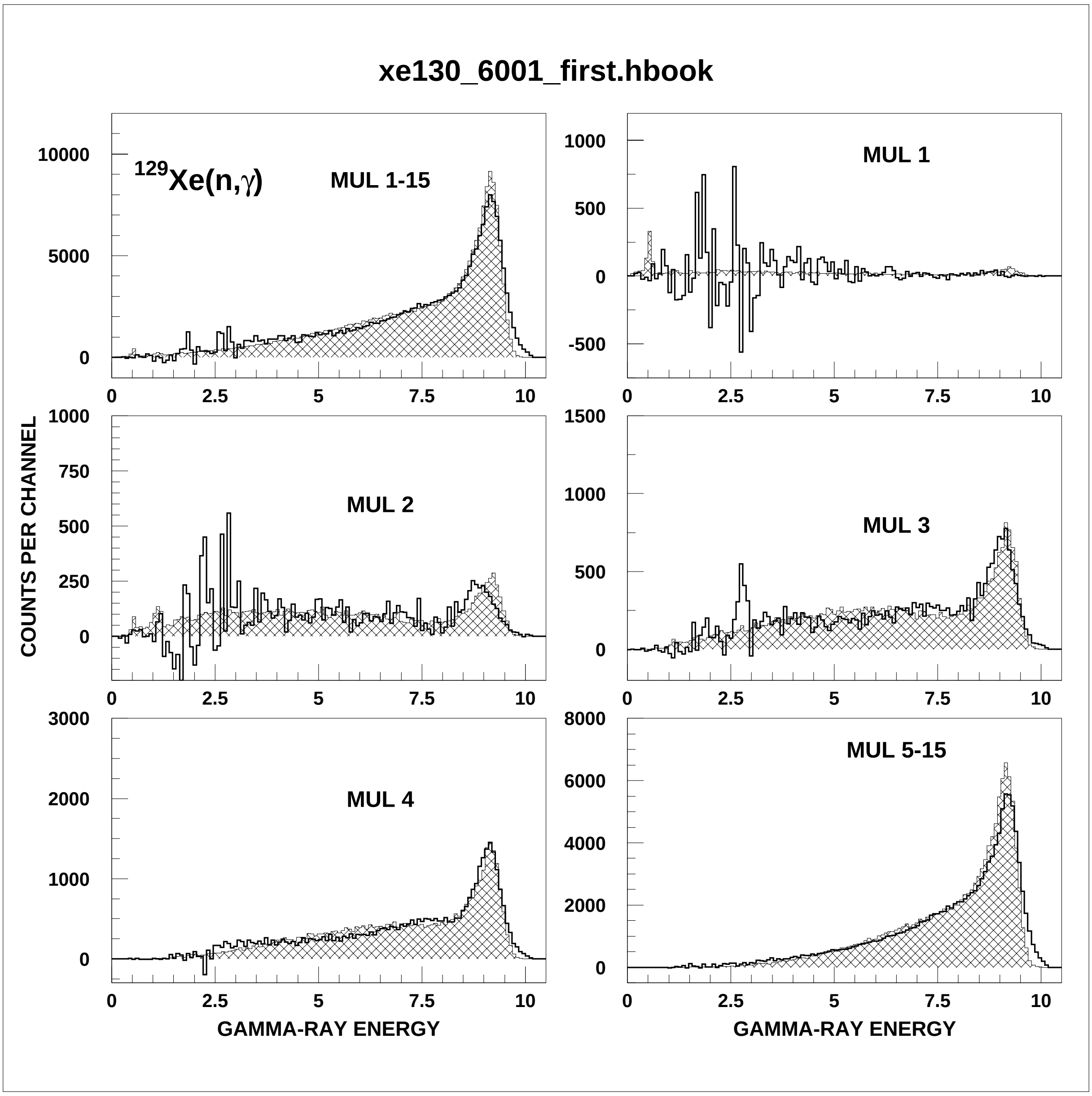

Figure 12: Simulated sum energy spectra for capture in ^{129}Xe for different multiplicities (hatched) compared to the experimental spectra shown in Fig. 9 (histogram).

tal spectrum in the upper left corner is perfectly reproduced all the way down to the experimental threshold at 1.6 MeV.

In all previous measurements with the Karlsruhe 4πBaF$_2$ detector the gold spectrum represented a longstanding problem. The full energy peak was always considerably broader than for practically all 50 isotopes measured so far. Moreover, the peak energy deviated by about 300 keV from the binding energy of the captured neutron, whereas this correlation was consistently confirmed in all other cases over a wide range between 4.5 and 9 MeV.

In principle, this effect could have been due to the 312 keV isomer in ^{198}Au, which

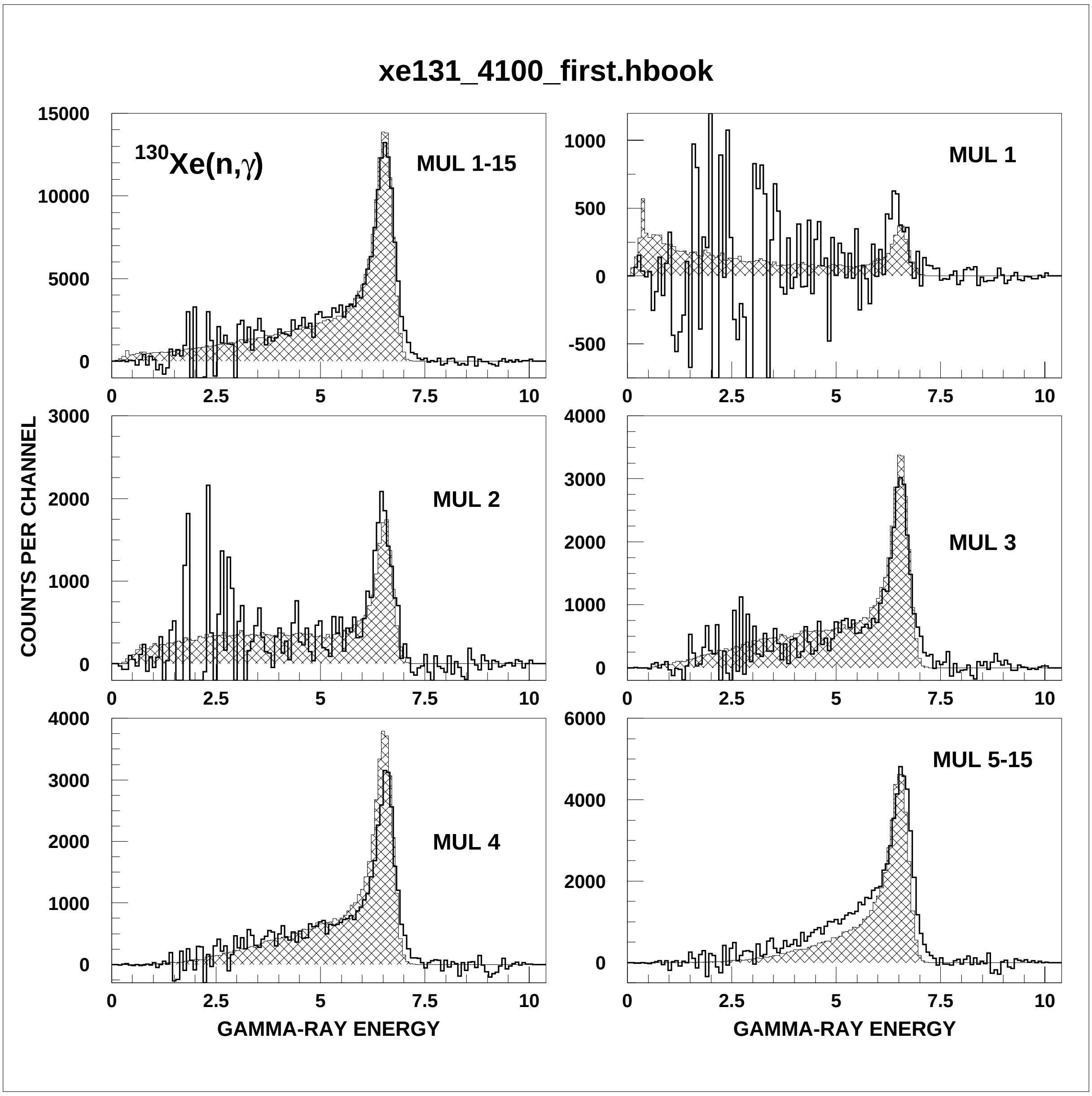

Figure 13: Simulated sum energy spectra for capture in ^{130}Xe for different multiplicities (hatched) compared to the experimental spectra shown in Fig. 9 (histogram).

has a half-life of 124 ns, much longer than the time window of ≈30 ns for accepting single events. However, this isomer was found to be too weakly populated to account for the observed effect [24]. The present GEANT simulations have shown that the shift as well as the broadening of the full energy peak in the gold spectrum is caused by conversion electrons. Converted transitions occur in a significant fraction of capture cascades in ^{198}Au as a consequence of the high atomic number and the high level density. Being absorbed in the sample or the reflector layers, these electrons do not contribute to the barium fluoride signals and are therefore also missing in the sum energy signal peak.

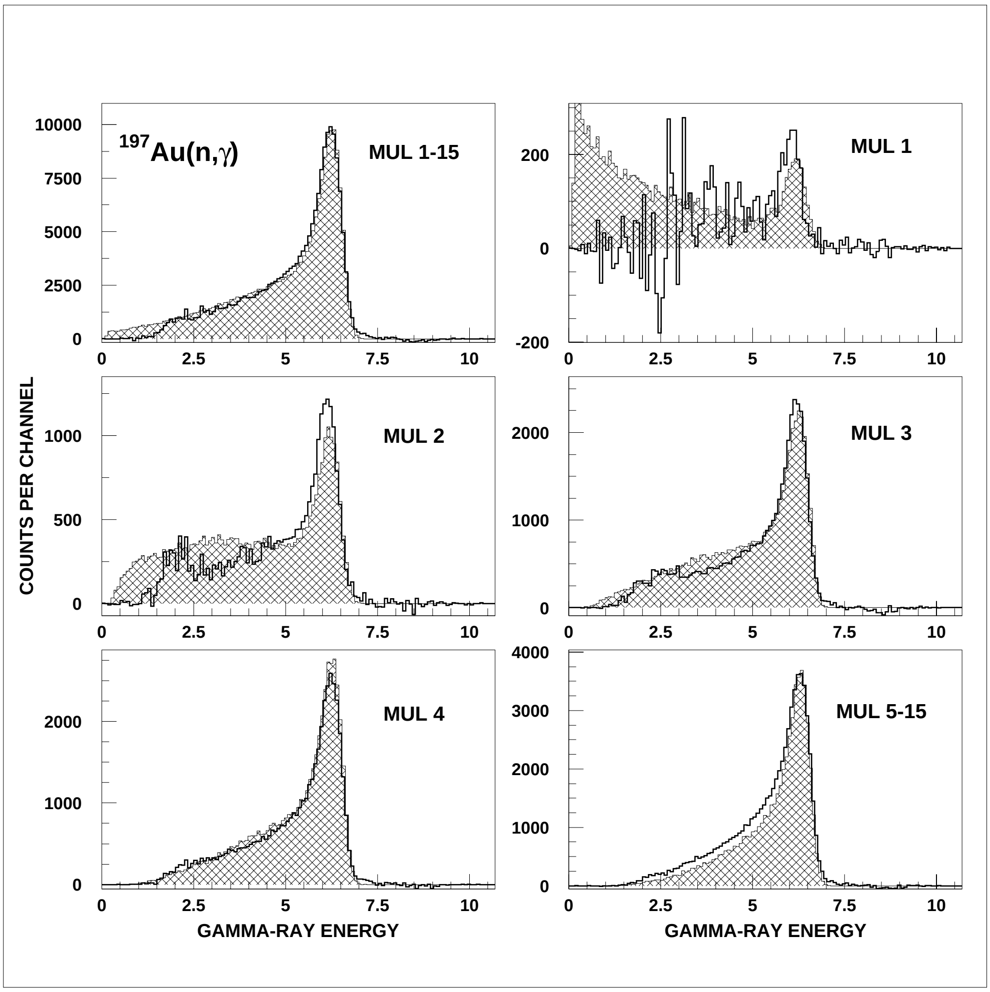

Figure 14: Simulated sum energy spectra for capture in ^{197}Au for different multiplicities (hatched) compared to the experimental spectra (histogram).

In order to demonstrate this effect the simulation of capture in gold was repeated converting artificially all conversion electrons into gamma-rays. The resulting spectra in Fig. 15 exhibit a full energy peak which is much sharper and shifted to higher energies compared to the measured distribution. Moreover, this simulation fails clearly to reproduce the experimental multiplicity distribution.

This significant role of converted transitions has practically no consequences for the cross sections derived in the present experiment since the efficiency is determined by the comparably low threshold in γ-ray energy, essentially independent of the total cascade energy. However, other experimental techniques for the measurement of (n,γ) cross sections, e.g. Moxon-Rae detectors or C_6D_6 detectors using the pulse height weighting technique, are explicitely based on the assumption that the total cascade energy corresponds to the binding energy of the captured neutrons. While this assumption is justified for the isotopes with low level densities it is certainly not valid for gold and other heavy nuclei. In the past, proper corrections for the effect of converted transitions have always been neglected. This may well be a recent for discrepancies among previous data, in particular since many experiments were using gold as a cross section standard.

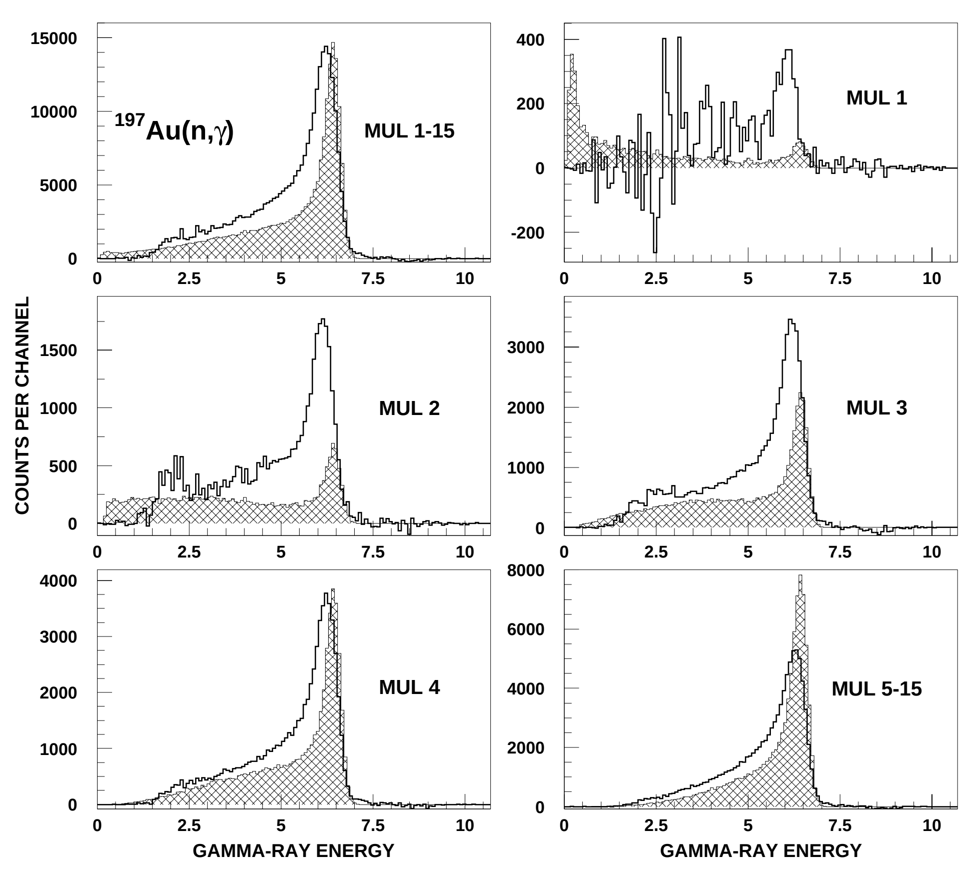

Figure 15: Simulated sum energy spectra for capture in ^{197}Au (hatched) if all conversion electrons are treated as γ-rays. Comparison with the experimental spectra (histogram) shows that this assumption implies severe discrepancies.

A second feature of the GEANT simulations is that they provide a completely independent way of determining the correction for the fraction of unobserved capture events. This is particularly important since the uncertainty of this correction usually dominates the systematic uncertainties in the measurements with the 4π BaF$_2$ detector. From the simulated total spectra (upper left panels in Figs. 11,12,13,and 14) the respective fraction of events below a given threshold energy is listed in Table 10 together with the corresponding correction factors F$_1$. At the 1.6 and 1.7 MeV thresholds of the present experiment the F$_1$ values obtained in the simulations and the results of the corrections determined by the standard procedure (Table 6) agree on average within 0.5%. This is a remarkable confirmation for the previously adopted procedure since the two approaches are completely independent of each other.

Table 10: FRACTION OF UNDETECTED CAPTURE EVENTS, f (%), AND THE RELATED CORRECTION FACTORS F_1.[a]

	Threshold in Sum Energy (MeV)			
	1.5	1.6	1.7	2.0
f(Au)	4.19			6.68
f(^{128}Xe)	3.58			5.45
f(^{129}Xe)	1.13			1.81
f(^{130}Xe)	4.08			6.20
F_1(^{128}Xe/Au)	0.994	0.993	0.991	0.987
F_1(^{129}Xe/Au)	0.969	0.965	0.961	0.950
F_1(^{130}Xe/Au)	0.999	0.998	0.997	0.995

[a] derived from the GEANT simulation

5 RESULTS FOR THE NEUTRON CAPTURE CROSS SECTIONS

The measured neutron capture cross section ratios of the investigated Xe isotopes, and of ^{197}Au are listed in Tables 11 to 16 together with the respective statistical uncertainties. The data are given for all runs and for the different samples as well as for both evaluations discussed in Sec. 3. The last column in each table contains the weighted average, the weight being determined by the inverse of the squared statistical uncertainties Since the cross section ratios depend weakly on energy, the averages for the energy interval from 30 to 80 keV are also included for a better comparison of the individual results The agreement of results obtained in different runs, evaluations, or with different samples provides an important verification of the respective corrections and hence for the reliability of the method.

As in the previous measurements with the 4π BaF_2 detector [7, 8, 9], the final cross section ratios were adopted from evaluation 2. The respective mean values are compiled for all runs in Table 17 together with the statistical, systematic, and total uncertainties. The energy bins are sufficiently fine to avoid systematic uncertainties in the calculation of the Maxwellian averaged cross sections (Sec. 7). The final statistical uncertainties of the cross section ratios are less than 2% in the energy range from 15 to 100 keV for all isotopes, but reach 8 to 16% in the lowest energy bins. The systematic uncertainties are 1.1 - 1.8%

The experimental ratios were converted into absolute cross sections using the gold data of Macklin [25] after normalization by a factor of 0.989 to the absolute value of Ratynski and Käppeler [26] (Table 18). The uncertainties of the resulting cross sections can be obtained by adding the 1.5% uncertainty of the reference cross section to the uncertainties of the respective ratios. The final values for the cross sections in dependence of the neutron energy are shown in Figs. 16 and 17.

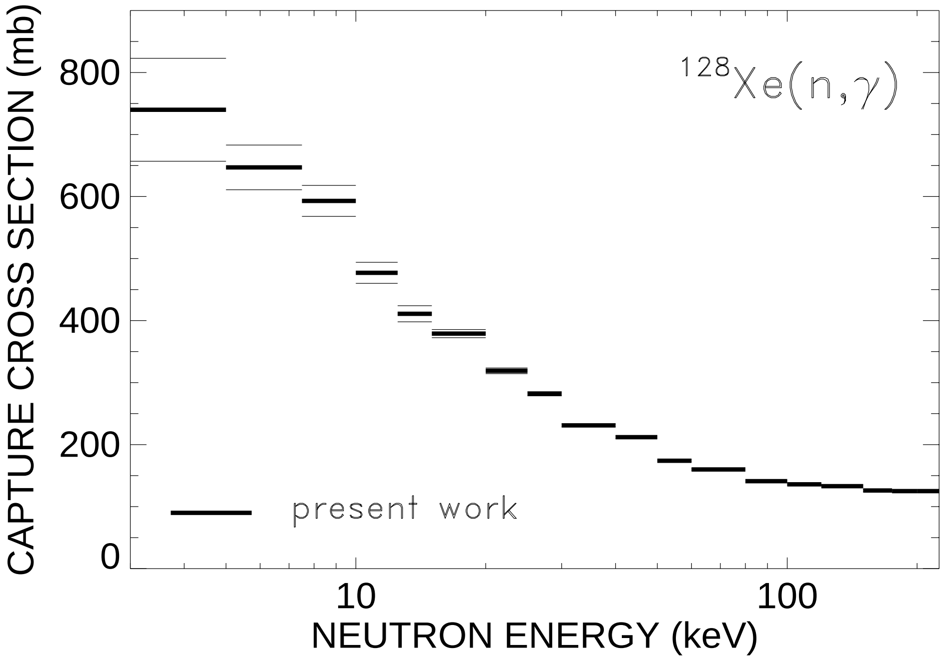

Figure 16: The neutron capture cross section of ^{128}Xe.

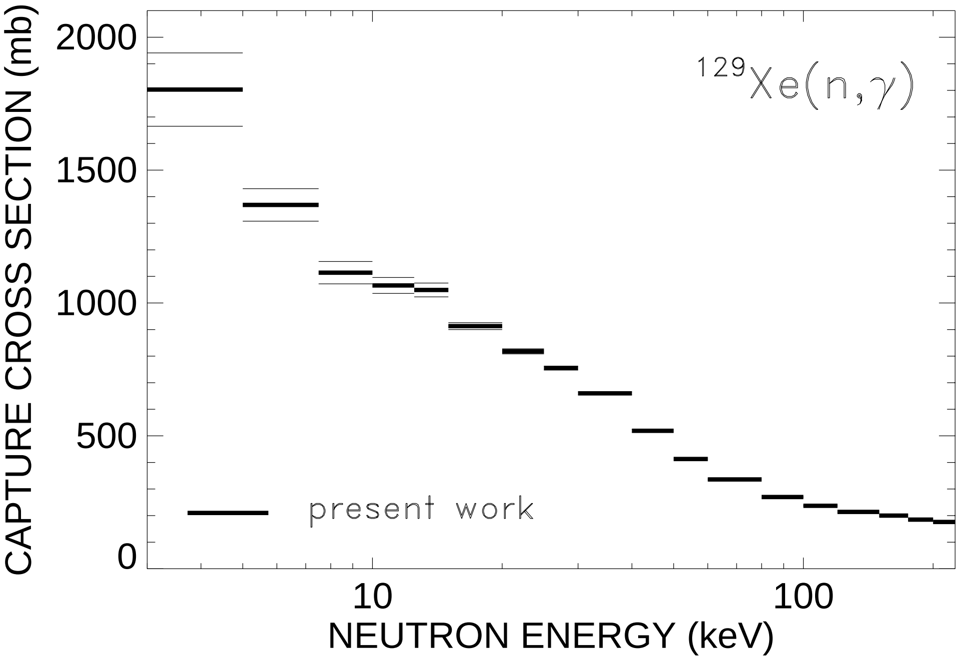

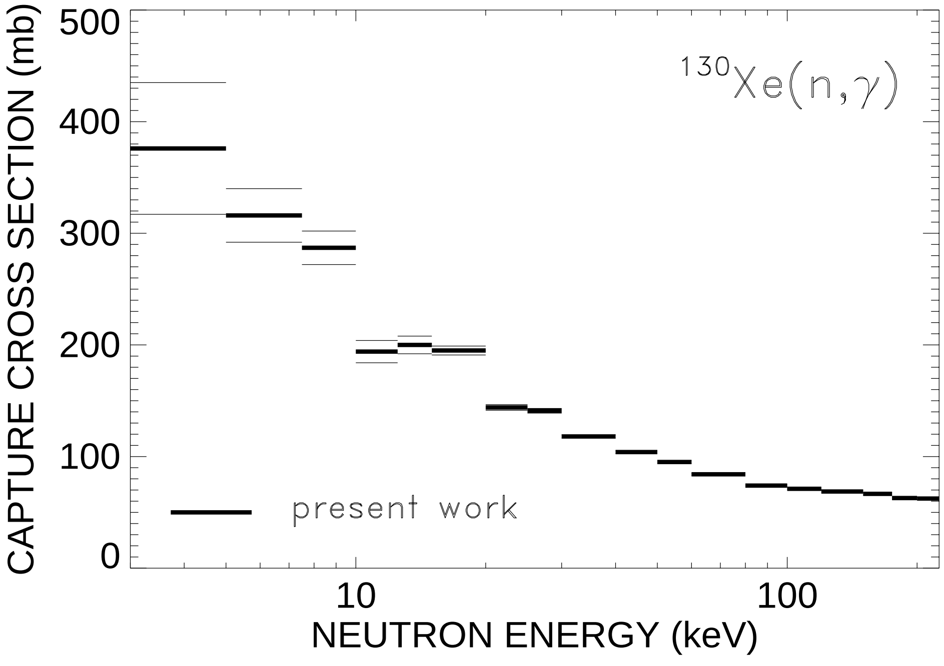

Figure 17: The neutron capture cross sections of ^{129}Xe and ^{130}Xe.

Table 11: CROSS SECTION RATIOS $\sigma(^{128}\mathrm{Xe})/\sigma(^{197}\mathrm{Au})$ OBTAINED IN EVALUATION 1 AND STATISTICAL UNCERTAINTIES (in %)

Energy Bin (keV)	Run I				Run II			
Sample Number	10		11		10		11	
3 – 5	0.2358	46.	0.3019	27.	0.3562	36.	0.3872	27.
5 – 7.5	0.3695	18.	0.3767	14.	0.3880	19.	0.3958	15.
7.5 – 10	0.5408	13.	0.4551	12.	0.5879	14.	0.4967	13.
10 – 12.5	0.4318	12.	0.4584	8.9	0.4381	15.	0.4221	12.
12.5 – 15	0.4763	10.	0.4777	8.1	0.4810	12.	0.4212	11.
15 – 20	0.5026	5.6	0.4701	4.5	0.5258	6.6	0.4778	5.9
20 – 25	0.5471	4.7	0.5112	3.8	0.4975	5.7	0.5415	4.6
25 – 30	0.5130	4.0	0.4818	3.3	0.4749	4.7	0.4761	3.9
30 – 40	0.4700	3.5	0.4457	2.7	0.4493	3.5	0.4543	2.9
40 – 50	0.5006	3.4	0.4793	2.7	0.4768	3.4	0.4931	2.8
50 – 60	0.4570	3.3	0.4257	2.6	0.4460	3.5	0.4556	2.9
60 – 80	0.4672	3.1	0.4382	2.4	0.4522	2.9	0.4457	2.4
80 – 100	0.4831	3.1	0.4611	2.4	0.4683	2.8	0.4734	2.4
100 – 120	0.4779	3.2	0.4552	2.5	0.4684	2.8	0.4799	2.4
120 – 150	–	–	–	–	0.4801	2.7	0.4971	2.2
150 – 175	–	–	–	–	0.4754	2.8	0.4764	2.3
175 – 200	–	–	–	–	0.4917	2.9	0.4935	2.4
200 – 225	–	–	–	–	0.4956	3.4	0.5049	2.9
30 – 80	0.4737	2.9	0.4472	2.2	0.4561	2.3	0.4622	1.9

Energy Bin (keV)	Run III				Average	
Sample Number	10		11			
3 – 5	0.2251	62.	0.2861	53.	0.3244	15.
5 – 7.5	0.5317	20.	0.4336	23.	0.4071	7.2
7.5 – 10	0.5182	16.	0.4173	17.	0.5037	5.7
10 – 12.5	0.3827	15.	0.4952	12.	0.4450	4.9
12.5 – 15	0.4253	11.	0.4809	10.	0.4631	4.2
15 – 20	0.5043	6.1	0.5296	6.0	0.4974	2.3
20 – 25	0.5485	5.0	0.5575	5.2	0.5330	1.9
25 – 30	0.5162	4.3	0.5199	4.4	0.4953	1.6
30 – 40	0.4519	3.7	0.4938	3.7	0.4587	1.3
40 – 50	0.4879	3.6	0.5023	3.7	0.4891	1.3
50 – 60	0.4552	3.6	0.4656	3.7	0.4484	1.3
60 – 80	0.4676	3.3	0.4700	3.4	0.4536	1.2
80 – 100	0.4642	3.3	0.4767	3.4	0.4704	1.2
100 – 120	0.4599	3.5	0.4696	3.6	0.4689	1.2
120 – 150	–	–	–	–	0.4902	1.7
150 – 175	–	–	–	–	0.4760	1.8
175 – 200	–	–	–	–	0.4927	1.8
200 – 225	–	–	–	–	0.5011	2.2
30 – 80	0.4657	3.2	0.4829	3.2	0.4625	1.0

Table 12: CROSS SECTION RATIOS $\sigma(^{128}\mathrm{Xe})/\sigma(^{197}\mathrm{Au})$ OBTAINED IN EVALUATION 2 AND STATISTICAL UNCERTAINTIES (in %)

Energy Bin (keV)	Run I				Run II			
Sample Number	10		11		10		11	
3 – 5	0.2587	28.	0.2912	20.	0.3342	37.	0.3362	29.
5 – 7.5	0.3768	13.	0.3798	10.	0.3795	17.	0.3765	14.
7.5 – 10	0.4760	9.7	0.4350	8.6	0.5360	11.	0.4960	10.
10 – 12.5	0.4328	8.3	0.4366	6.8	0.4412	11.	0.4382	9.2
12.5 – 15	0.4712	7.5	0.4876	6.1	0.4459	11.	0.4865	8.3
15 – 20	0.5202	4.0	0.5005	3.4	0.5229	5.2	0.4724	4.6
20 – 25	0.5227	3.5	0.5248	2.9	0.5033	4.5	0.5356	3.6
25 – 30	0.4890	3.0	0.4919	2.5	0.4742	3.6	0.4701	3.0
30 – 40	0.4438	2.5	0.4584	2.0	0.4597	2.7	0.4578	2.3
40 – 50	0.4680	2.4	0.4880	2.0	0.4918	2.6	0.4883	2.2
50 – 60	0.4288	2.4	0.4306	2.0	0.4494	2.6	0.4476	2.2
60 – 80	0.4466	2.1	0.4530	1.7	0.4568	2.2	0.4481	1.9
80 – 100	0.4606	2.1	0.4752	1.7	0.4673	2.1	0.4672	1.8
100 – 120	0.4486	2.3	0.4616	1.9	0.4737	2.1	0.4831	1.8
120 – 150	–	–	–	–	0.4804	2.0	0.4900	1.7
150 – 175	–	–	–	–	0.4835	2.1	0.4757	1.8
175 – 200	–	–	–	–	0.4924	2.2	0.4934	1.9
200 – 225	–	–	–	–	0.4977	2.7	0.5073	2.3
30 – 80	0.4468	1.9	0.4575	1.5	0.4644	1.7	0.4605	1.4

Energy Bin (keV)	Run III				Average	
Sample Number	10		11			
3 – 5	0.3204	31.	0.4315	26.	0.3262	11.
5 – 7.5	0.3767	16.	0.3497	16.	0.3745	5.6
7.5 – 10	0.5089	12.	0.5156	11.	0.4878	4.2
10 – 12.5	0.4181	9.8	0.5046	8.1	0.4470	3.5
12.5 – 15	0.4335	8.0	0.4627	7.3	0.4682	3.1
15 – 20	0.5180	4.5	0.5472	4.3	0.5127	1.7
20 – 25	0.5550	3.6	0.5469	3.6	0.5322	1.4
25 – 30	0.5228	3.1	0.5119	3.1	0.4937	1.2
30 – 40	0.4598	2.7	0.4872	2.5	0.4607	1.0
40 – 50	0.5051	2.6	0.5032	2.5	0.4901	1.0
50 – 60	0.4664	2.6	0.4638	2.5	0.4457	1.0
60 – 80	0.4819	2.3	0.4682	2.2	0.4575	0.8
80 – 100	0.4812	2.3	0.4776	2.2	0.4713	0.8
100 – 120	0.4742	2.5	0.4709	2.4	0.4693	0.9
120 – 150	–	–	–	–	0.4859	1.3
150 – 175	–	–	–	–	0.4790	1.4
175 – 200	–	–	–	–	0.4930	1.4
200 – 225	–	–	–	–	0.5032	1.7
30 – 80	0.4783	2.1	0.4806	2.0	0.4635	0.7

Table 13: CROSS SECTION RATIOS $\sigma(^{129}\mathrm{Xe})/\sigma(^{197}\mathrm{Au})$ OBTAINED IN EVALUATION 1 AND STATISTICAL UNCERTAINTIES (in %)

Energy Bin (keV)	Run I				Run II		Run III		Average	
Sample Number	7		8		7		7			
3 – 5	0.4476	24.	0.6177	19.	0.9962	18.	1.5463	18.	0.9666	11.
5 – 7.5	0.4473	15.	0.7129	11.	0.9364	10.	1.2424	13.	0.8533	6.2
7.5 – 10	0.5070	13.	0.9479	9.1	1.1394	10.	1.1744	10.	0.9875	5.3
10 – 12.5	0.7580	7.9	1.1073	6.7	0.9324	8.9	1.2124	7.6	1.0202	3.9
12.5 – 15	1.0274	6.5	1.3892	5.9	1.1738	7.5	1.2097	6.2	1.2116	3.2
15 – 20	1.0740	3.5	1.2537	3.4	1.2433	4.3	1.3172	3.8	1.2177	1.8
20 – 25	1.3082	2.9	1.4125	2.9	1.3755	3.5	1.4377	3.2	1.3826	1.6
25 – 30	1.2930	2.4	1.3592	2.4	1.3236	2.9	1.3965	2.6	1.3425	1.3
30 – 40	1.3024	2.0	1.3537	2.0	1.2888	2.1	1.3619	2.2	1.3266	1.0
40 – 50	1.2090	2.0	1.2147	2.0	1.1882	2.2	1.2099	2.2	1.2060	1.0
50 – 60	1.0712	1.9	1.0585	1.9	1.0787	2.2	1.0748	2.2	1.0701	1.0
60 – 80	0.9533	1.8	0.9410	1.8	0.9755	1.9	0.9803	2.0	0.9611	0.9
80 – 100	0.8916	1.8	0.9034	1.8	0.9279	1.8	0.9102	2.0	0.9079	0.9
100 – 120	0.8116	1.9	0.8074	1.9	0.8521	1.9	0.8484	2.2	0.8289	1.0
120 – 150	–	–	–	–	0.7923	1.8	–	–	0.7923	1.8
150 – 175	–	–	–	–	0.7635	1.8	–	–	0.7635	1.8
175 – 200	–	–	–	–	0.7407	1.9	–	–	0.7407	1.9
200 – 225	–	–	–	–	0.7179	2.4	–	–	0.7179	2.4
30 – 80	1.1340	1.6	1.1420	1.6	1.1328	1.5	1.1567	1.8	1.1410	0.8

Table 14: CROSS SECTION RATIOS $\sigma(^{129}\mathrm{Xe})/\sigma(^{197}\mathrm{Au})$ OBTAINED IN EVALUATION 2 AND STATISTICAL UNCERTAINTIES (in %)

Energy Bin (keV)	Run I				Run II	
Sample Number	7		8		7	
3 – 5	0.5566	15.	0.5990	14.	0.9419	18.
5 – 7.5	0.5726	9.1	0.6934	8.0	0.9670	9.4
7.5 – 10	0.6707	7.8	0.8858	6.7	1.0263	8.0
10 – 12.5	0.8254	5.6	1.0583	5.0	1.0100	6.9
12.5 – 15	1.0857	4.9	1.3204	4.6	1.2472	6.2
15 – 20	1.1255	2.7	1.2552	2.6	1.2694	3.4
20 – 25	1.3035	2.3	1.3737	2.2	1.4033	2.8
25 – 30	1.2752	1.9	1.3277	1.9	1.3250	2.2
30 – 40	1.2888	1.5	1.3275	1.5	1.3150	1.7
40 – 50	1.1904	1.5	1.2002	1.5	1.1902	1.7
50 – 60	1.0466	1.5	1.0426	1.5	1.0729	1.7
60 – 80	0.9499	1.3	0.9416	1.3	0.9856	1.4
80 – 100	0.8849	1.3	0.9017	1.3	0.9303	1.4
100 – 120	0.7905	1.4	0.7910	1.4	0.8490	1.5
120 – 150	–	–	–	–	0.7801	1.4
150 – 175	–	–	–	–	0.7578	1.5
175 – 200	–	–	–	–	0.7305	1.5
200 – 225	–	–	–	–	0.7101	2.0
30 – 80	1.1189	1.1	1.1280	1.1	1.1409	1.1

Energy Bin (keV)	Run III		Average	
Sample Number	7			
3 – 5	1.0958	14.	0.7953	7.7
5 – 7.5	0.9614	8.7	0.7926	4.5
7.5 – 10	1.0870	7.5	0.9166	3.8
10 – 12.5	1.0892	5.5	0.9997	2.8
12.5 – 15	1.1389	4.5	1.1948	2.5
15 – 20	1.3065	2.8	1.2351	1.4
20 – 25	1.3848	2.3	1.3627	1.2
25 – 30	1.3614	1.9	1.3218	1.0
30 – 40	1.3476	1.5	1.3196	0.8
40 – 50	1.2044	1.5	1.1965	0.8
50 – 60	1.0813	1.5	1.0595	0.8
60 – 80	0.9761	1.4	0.9618	0.7
80 – 100	0.9079	1.4	0.9051	0.7
100 – 120	0.8384	1.5	0.8161	0.7
120 – 150	–	–	0.7801	1.4
150 – 175	–	–	0.7578	1.5
175 – 200	–	–	0.7305	1.5
200 – 225	–	–	0.7101	2.0
30 – 80	1.1524	1.2	1.1344	0.6

Table 15: CROSS SECTION RATIOS $\sigma(^{130}\text{Xe})/\sigma(^{197}\text{Au})$ OBTAINED IN EVALUATION 1 AND STATISTICAL UNCERTAINTIES (in %)

Energy Bin (keV)	Run I				Run II			
Sample Number	12		13		12		14	
3 – 5	0.1724	35.	0.2087	38.	0.2289	31.	0.1388	53.
5 – 7.5	0.1720	21.	0.1735	27.	0.2146	19.	0.1476	28.
7.5 – 10	0.2463	14.	0.2699	17.	0.2355	18.	0.2856	16.
10 – 12.5	0.1987	13.	0.2073	16.	0.2270	15.	0.2200	16.
12.5 – 15	0.2738	9.4	0.2218	14.	0.2503	12.	0.2489	13.
15 – 20	0.2638	5.5	0.2517	7.3	0.2648	6.8	0.2686	7.1
20 – 25	0.2338	5.2	0.2368	6.7	0.2214	6.5	0.2506	6.2
25 – 30	0.2607	4.0	0.2308	5.6	0.2269	5.0	0.2416	5.0
30 – 40	0.2369	3.4	0.2191	4.8	0.2413	3.5	0.2373	3.7
40 – 50	0.2406	3.4	0.2305	4.7	0.2461	3.5	0.2456	3.7
50 – 60	0.2480	3.3	0.2232	4.5	0.2530	3.4	0.2429	3.6
60 – 80	0.2442	3.0	0.2259	4.2	0.2430	2.9	0.2444	3.1
80 – 100	0.2566	3.0	0.2360	4.2	0.2546	2.9	0.2562	3.0
100 – 120	0.2531	3.2	0.2264	4.4	0.2491	2.9	0.2521	3.0
120 – 150	–	–	–	–	0.2534	2.7	0.2619	2.8
150 – 175	–	–	–	–	0.2542	2.8	0.2540	2.9
175 – 200	–	–	–	–	0.2581	2.9	0.2521	3.1
200 – 225	–	–	–	–	0.2541	3.5	0.2621	3.6
30 – 80	0.2424	2.9	0.2247	4.0	0.2459	2.4	0.2426	2.5

Energy Bin (keV)	Run III				Average	
Sample Number	12		14			
3 – 5	0.0633	99.	0.0812	99.	0.1890	19.
5 – 7.5	0.2499	22.	0.1850	31.	0.1963	9.7
7.5 – 10	0.2424	18.	0.2069	21.	0.2513	6.9
10 – 12.5	0.2642	12.	0.1431	22.	0.2199	6.2
12.5 – 15	0.2495	11.	0.2016	13.	0.2463	4.8
15 – 20	0.3121	5.7	0.2676	6.5	0.2738	2.6
20 – 25	0.2529	5.5	0.2382	5.9	0.2395	2.4
25 – 30	0.2605	4.5	0.2572	4.8	0.2487	2.0
30 – 40	0.2519	3.8	0.2463	4.1	0.2399	1.6
40 – 50	0.2546	3.7	0.2477	4.0	0.2449	1.5
50 – 60	0.2566	3.7	0.2501	4.0	0.2471	1.5
60 – 80	0.2494	3.4	0.2476	3.7	0.2434	1.4
80 – 100	0.2573	3.4	0.2507	3.7	0.2533	1.4
100 – 120	0.2526	3.6	0.2447	3.9	0.2482	1.4
120 – 150	–	–	–	–	0.2575	2.0
150 – 175	–	–	–	–	0.2541	2.0
175 – 200	–	–	–	–	0.2552	2.1
200 – 225	–	–	–	–	0.2579	2.5
30 – 80	0.2531	3.2	0.2479	3.5	0.2438	1.4

Table 16: CROSS SECTION RATIOS $\sigma(^{130}\mathrm{Xe})/\sigma(^{197}\mathrm{Au})$ OBTAINED IN EVALUATION 2 AND STATISTICAL UNCERTAINTIES (in %)

Energy Bin (keV)	Run I				Run II				Run III				Average	
Sample Number	12		13		12		14		12		14			
3 – 5	0.1892	23.	0.1674	37.	0.1373	50.	0.1601	44.	0.1255	45.	0.0568	99.	0.1660	16.
5 – 7.5	0.1828	14.	0.2126	18.	0.1862	19.	0.1726	21.	0.1808	19.	0.1323	27.	0.1832	7.7
7.5 – 10	0.2405	10.	0.2748	13.	0.2202	14.	0.2470	13.	0.2117	15.	0.1948	17.	0.2358	5.4
10 – 12.5	0.1675	11.	0.1786	15.	0.1898	14.	0.2180	12.	0.1768	12.	0.1544	15.	0.1815	5.3
12.5 – 15	0.2306	8.2	0.2038	13.	0.2619	9.9	0.2545	10.	0.2218	8.2	0.1859	10.	0.2278	4.0
15 – 20	0.2557	4.3	0.2759	5.6	0.2644	5.4	0.2504	5.8	0.2735	4.5	0.2618	5.0	0.2636	2.0
20 – 25	0.2289	4.0	0.2507	5.2	0.2290	5.0	0.2570	4.7	0.2459	4.0	0.2349	4.5	0.2405	1.8
25 – 30	0.2512	3.1	0.2493	4.2	0.2290	3.9	0.2391	3.9	0.2534	3.2	0.2531	3.6	0.2469	1.5
30 – 40	0.2250	2.6	0.2328	3.5	0.2378	2.8	0.2333	2.9	0.2454	2.6	0.2384	3.0	0.2355	1.2
40 – 50	0.2313	2.5	0.2393	3.4	0.2425	2.7	0.2377	2.8	0.2422	2.6	0.2448	2.9	0.2394	1.1
50 – 60	0.2379	2.4	0.2381	3.3	0.2493	2.6	0.2390	2.8	0.2486	2.5	0.2505	2.9	0.2440	1.1
60 – 80	0.2355	2.2	0.2447	3.0	0.2419	2.3	0.2392	2.3	0.2407	2.3	0.2458	2.6	0.2407	1.0
80 – 100	0.2452	2.2	0.2530	3.0	0.2490	2.2	0.2469	2.3	0.2483	2.3	0.2473	2.7	0.2480	1.0
100 – 120	0.2414	2.3	0.2438	3.1	0.2517	2.2	0.2439	2.3	0.2463	2.5	0.2417	2.9	0.2452	1.0
120 – 150	–	–	–	–	0.2493	2.1	0.2519	2.1	–	–	–	–	0.2506	1.5
150 – 175	–	–	–	–	0.2556	2.2	0.2497	2.2	–	–	–	–	0.2527	1.6
175 – 200	–	–	–	–	0.2531	2.3	0.2437	2.4	–	–	–	–	0.2486	1.6
200 – 225	–	–	–	–	0.2481	2.8	0.2541	2.8	–	–	–	–	0.2510	2.0
30 – 80	0.2324	2.0	0.2387	2.7	0.2429	1.7	0.2373	1.8	0.2442	2.0	0.2449	2.4	0.2399	0.8

Table 17: FINAL NEUTRON CAPTURE CROSS SECTION RATIOS OF ^{128}Xe, ^{129}Xe, AND ^{130}Xe RELATIVE TO ^{197}Au

Energy Bin[a]	$\frac{\sigma(^{128}Xe)}{\sigma(^{197}Au)}$	Uncertainty (%)			$\frac{\sigma(^{129}Xe)}{\sigma(^{197}Au)}$	Uncertainty (%)			$\frac{\sigma(^{130}Xe)}{\sigma(^{197}Au)}$	Uncertainty (%)		
(keV)		stat	sys	tot		stat	sys	tot		stat	sys	tot
3 – 5	0.3262	11.	1.1	11.	0.7953	7.7	1.8	7.9	0.1660	16.	1.1	16.
5 – 7.5	0.3745	5.6	1.1	5.7	0.7926	4.5	1.8	4.8	0.1832	7.7	1.1	7.8
7.5 – 10	0.4878	4.2	1.1	4.3	0.9166	3.8	1.8	4.2	0.2358	5.4	1.1	5.5
10 – 12.5	0.4470	3.5	1.1	3.7	0.9997	2.8	1.8	3.3	0.1815	5.3	1.1	5.4
12.5 – 15	0.4682	3.1	1.1	3.3	1.1948	2.5	1.8	3.1	0.2278	4.0	1.1	4.1
15 – 20	0.5127	1.7	1.1	2.0	1.2351	1.4	1.8	2.3	0.2636	2.1	1.1	2.4
20 – 25	0.5322	1.4	1.1	1.8	1.3627	1.2	1.8	2.2	0.2405	1.8	1.1	2.1
25 – 30	0.4937	1.2	1.1	1.6	1.3218	1.0	1.8	2.1	0.2469	1.5	1.1	1.9
30 – 40	0.4607	1.0	1.1	1.5	1.3196	0.8	1.8	2.0	0.2355	1.2	1.1	1.6
40 – 50	0.4901	1.0	1.1	1.5	1.1965	0.8	1.8	2.0	0.2394	1.1	1.1	1.6
50 – 60	0.4457	1.0	1.1	1.5	1.0595	0.8	1.8	2.0	0.2440	1.1	1.1	1.6
60 – 80	0.4575	0.8	1.1	1.4	0.9618	0.7	1.8	1.9	0.2407	1.0	1.1	1.5
80 – 100	0.4713	0.8	1.1	1.4	0.9051	0.7	1.8	1.9	0.2480	1.0	1.1	1.5
100 – 120	0.4693	0.9	1.1	1.4	0.8161	0.7	1.8	1.9	0.2452	1.0	1.1	1.5
120 – 150	0.4859	1.3	1.1	1.7	0.7801	1.4	1.8	2.3	0.2506	1.5	1.1	1.9
150 – 175	0.4790	1.4	1.1	1.8	0.7578	1.5	1.8	2.3	0.2527	1.6	1.1	1.9
175 – 200	0.4930	1.4	1.1	1.8	0.7305	1.5	1.8	2.3	0.2486	1.6	1.1	1.9
200 – 225	0.5032	1.7	1.1	2.0	0.7101	2.0	1.8	2.7	0.2510	2.0	1.1	2.3

[a] Energy bins as used for calculating the Maxwellian averaged cross section

Table 18: NEUTRON CAPTURE CROSS SECTIONS OF ^{128}Xe, ^{129}Xe, AND ^{130}Xe (in mb)

Energy Bin[a] (keV)	$\sigma(^{197}\text{Au})$[b]	$\sigma(^{128}\text{Xe})$	$\sigma(^{129}\text{Xe})$	$\sigma(^{130}\text{Xe})$
3 – 5	2266.7	739.5	1803.	376.2
5 – 7.5	1726.7	646.7	1369.	316.3
7.5 – 10	1215.7	593.0	1114.	286.6
10 – 12.5	1066.7	476.9	1066.	193.6
12.5 – 15	878.0	411.1	1049.	200.0
15 – 20	738.8	378.8	912.5	194.7
20 – 25	600.0	319.4	817.7	144.3
25 – 30	570.8	281.8	754.5	140.9
30 – 40	500.4	230.6	660.3	117.9
40 – 50	433.3	212.4	518.5	103.7
50 – 60	389.6	173.7	412.8	95.1
60 – 80	349.4	159.8	336.0	84.1
80 – 100	298.3	140.6	270.0	74.0
100 – 120	290.1	136.2	236.8	71.1
120 – 150	274.1	133.2	213.8	68.7
150 – 175	263.7	126.3	199.8	66.6
175 – 200	252.6	124.5	184.5	62.8
200 – 225	248.5	125.0	176.4	62.4

[a] As used for calculating the Maxwellian averaged cross sections

[b] Based on the ^{197}Au data from literature[25, 26]

6 DISCUSSION OF UNCERTAINTIES

The determination of statistical and systematic uncertainties in measurements with the 4π BaF_2 detector has been described in Refs. [1, 7, 8]. The following discussion emphasizes the particular aspects of the present experiment. The various uncertainties are compiled in Table 19.

The binding energy for the even xenon isotopes is sufficiently low for normalizing the scattering background via the peak due to capture in the odd barium isotopes in the sum energy region around 9 MeV (see Figs. 5 and 6). In this way, a reliable correction could be determined, resulting in negligible systematic uncertainties. For ^{129}Xe, however, the high binding energy required to normalize the scattering background at the peak due to capture on the even barium isotopes at 6.8 MeV. This feature being weaker and affected by the tail of the true capture events implies a non-neglible systematic uncertainty of 1% for the effect of scattered neutrons.

The systematic uncertainty due to the normalization of all spectra to equal neutron flux have been discussed previously and is given in Table 19. The 0.1% uncertainty usually related to the ±0.2 mm uncertainty of the flight path measurement was recently confirmed by comparing the resonance energies determined with the present setup [27] with the values obtained with much better resolution at ORELA [28]. Since the definition of the flight path was hampered by the spherical samples, a systematic uncertainty of 0.5% was adopted in the present experiment.

In the quality certificate of the enriched xenon gas chemical admixtures of other noble gases as well as of CO, CO_2, CH_4, O_2, N_2, and even H_2O were listed, however in most cases with upper limits of 0.005%. Traces of additional impurities might have been collected during the filling procedure although no evidence was detected neither from the vacuum conditions nor from any inconsistencies in the cross section data derived from different samples. In view of the very small contaminations and the fact that most of these light isotopes have tiny cross sections, a systematic uncertainty of 0.1% was considered for this correction.

Since the enrichment of all samples was close to 100% (Table 2), the corrections for isotopic impurities were correspondingly small. Following the usual prescription for evaluating the related uncertainties (see Refs. [10, 18] for example), all isotopic corrections in the present experiment are found to exhibit uncertainties of about 0.2%.

Because of the high enrichment the correction for multiple scattering and self-shielding was calculated assuming that the sample consisted only of the main isotope. The 0.3 and 0.4% uncertainties provided by the SESH code [19] for the even and odd samples respectively had to be increased, however, since the spherical samples were approximated by cylindrical shapes in these calculations. Since the results given in Table 9 are almost independent on the sample mass, the geometric approximation is also not expected to have a strong influence on this correction either. Therefore, a systematic uncertainty of 0.8% was assumed for all isotopes, about a factor of two larger than the uncertainties calculated by the SESH code.

The systematic uncertainties due to undetected events were discussed in detail for the gadolinium experiment [10], where uncertainties of 0.3% for the even and 0.8% for the odd isotope were estimated for the correction factor F_1. This estimate was based on two independent sets of calculated capture cascades, and was found to agree with the respective uncertainties quoted in previous measurements with the 4π BaF_2 detector [7, 8, 9]. It turned out that this uncertainty was mainly determined by the difference in binding energy between the investigated isotope and the gold standard, which is large for the odd, but small for the even gadolinium isotopes. For the dysprosium isotopes [18] it was verified, that using the experimental instead of the theoretical capture cascades essentially the same F_2 values were obtained, thus confirming the attributed uncertainties.

For Xe the binding energies of the even isotopes are similar to that of gold, but differ significantly for ^{129}Xe. Therefore an uncertainty of 0.4% was assumed for ^{128,130}Xe and 1.1% for ^{129}Xe. These uncertainties are also supported by the GEANT simulations, which yield correction factors F_1 (Table 10) that agree on average within 0.6% with the results listed in Table 6.

Table 19: SYSTEMATIC UNCERTAINTIES (%)

Background subtraction (^{129}Xe)	1.0
Flight path	0.5
Neutron flux normalization	0.2
Sample mass: elemental impurities	0.1
Isotopic composition	0.2
Multiple scattering and self–shielding: F_2	
cross section ratio	0.8
Undetected events: F_1	
cross section ratio (even/odd isotopes)	0.4/1.1
total systematic uncertainties	
$\sigma(^{128}\mathrm{Xe})/\sigma(\mathrm{Au})$	1.1
$\sigma(^{129}\mathrm{Xe})/\sigma(\mathrm{Au})$	1.8
$\sigma(^{130}\mathrm{Xe})/\sigma(\mathrm{Au})$	1.1

7 MAXWELLIAN AVERAGED CROSS SECTIONS

Maxwellian averaged cross sections were calculated in the same way as described in Refs. [1, 7]. The neutron energy range from 0 - 700 keV was divided into three intervals according to the origin of the adopted cross sections. The respective contributions I_x are given in Table 20. The main contribution, i.e. the interval I_2 from 3 to 225 keV, is provided by the present experiment (Table 18). These data were obtained with sufficient resolution to exclude systematic uncertainties that may result from a coarse energy grid.

The contribution I_1 was determined by normalizing the theoretical cross sections of Kopecky *et al.* [29] to the present data in the interval between 3 to 15 keV. The energy dependence of both data sets turned out to be in good agreement since consistent normalization factor were obtained for all five energy bins in this interval. Therefore, this contribution was based on the mean of the five intervals with an uncertainty of 5% being derived from the spread of these values.

The energy interval from 225 to 700 keV contributes very little to the Maxwellian average at typical *s*-process temperatures. Here, the data of Ref. [29] were normalized to the experimental cross sections in the energy range from 50 to 225 keV, and the corresponding uncertainties were assumed to increase from 2% at 225 keV to 10% at 700 keV neutron energy.

The systematic uncertainties of the Maxwellian averaged cross sections in Table 20 correspond to the uncertainties of the cross section ratios (Table 17) and include the respective contributions from the intervals I_1 and I_3. The 1.5% uncertainty of the gold standard was not considered since it cancels out in most applications of relevance for *s*-process studies. In general, the systematic uncertainties dominate over the statistical uncertainties except for the even isotopes at low thermal energies.

The present results at kT=30 keV are eventually compared in Table 21 with the previous semi-empirical estimates and with the compilations of Refs. [2, 30]. For these important isotopes the overall uncertainty could be improved by more than an order of magnitude to ≈2%. Accordingly, comparison of the $N_s < \sigma >$ values for ^{128}Xe and ^{130}Xe can now be used to reliably identify a possible branching of the s-process path. A detailed discussion of this possibility is in preparation.

Table 20: MAXWELLIAN AVERAGED NEUTRON CAPTURE CROSS SECTIONS OF THE XENON ISOTOPES.

^{128}Xe							
ΔE	0 - 3 keV	3 - 225 keV	225 - 700 keV	Thermal Spectrum			
Data:	from Ref. [29][a]	this work	from Ref. [29][a]				
kT	I_1	I_2	I_3	$<\sigma v>/v_T$ (mbarn)			
(keV)	(mbarn)	(mbarn)	(mbarn)		stat	sys[b]	tot
8	49.3±2.5	476.0±10.0	0.0	525.3	10.	5.8	12.
10	32.5±1.6	438.5±7.7	0.0	471.0	7.9	5.2	9.5
15	15.0±0.8	366.0±4.7	0.0	381.0	4.8	4.2	6.4
20	8.6±0.4	317.3±3.4	0.0	325.9	3.4	3.6	5.0
25	5.6±0.3	283.2±2.7	0.2	289.0	2.7	3.2	4.2
30	3.9±0.2	258.0±2.3	0.6	262.5	2.3	2.9	3.7
40	2.2±0.1	222.4±1.8	3.2±0.1	227.8	1.8	2.5	3.1
50	1.4±0.1	196.6±1.5	8.1±0.3	206.1	1.5	2.3	2.7
52	1.3±0.1	192.1±1.5	9.4±0.3	202.8	1.5	2.2	2.7
60	1.0±0.1	175.7±1.3	14.9±0.5	191.6	1.4	2.1	2.5
70	0.7±0.0	157.8±1.2	22.5±0.8	181.0	1.4	2.0	2.4
80	0.6±0.0	142.3±1.1	30.1±1.1	173.0	1.6	1.9	2.5
90	0.4±0.0	128.6±1.0	37.2±1.4	166.2	1.7	1.8	2.5
100	0.4±0.0	116.6±0.9	43.6±1.7	160.6	1.9	1.8	2.6
^{129}Xe							
ΔE	0 - 3 keV	3 - 225 keV	225 - 700 keV	Thermal Spectrum			
Data:	from Ref. [29][a]	this work	from Ref. [29][a]				
kT	I_1	I_2	I_3	$<\sigma v>/v_T$ (mbarn)			
(keV)	(mbarn)	(mbarn)	(mbarn)		stat	sys[b]	tot
8	173.2±8.7	1100.±17.	0.0	1273.	19.	23.	30.
10	114.8±5.7	1031.±13.	0.0	1146.	14.	21.	25.
15	53.5±2.7	878.8±8.4	0.0	932.3	8.8	17.	19.
20	30.8±1.5	762.1±6.2	0.0	792.9	6.4	14.	15.
25	20.0±1.0	672.4±4.9	0.2	692.6	5.0	12.	13.
30	14.0±0.7	602.1±4.1	0.9	617.0	4.2	11.	12.
40	8.0±0.4	498.7±3.2	4.4±0.1	511.1	3.2	9.2	9.7
50	5.2±0.3	424.9±2.6	11.1±0.3	441.2	2.6	7.9	8.3
52	4.8±0.2	412.4±2.5	12.8±0.4	430.0	2.5	7.7	8.1
60	3.6±0.2	368.1±2.3	20.0±0.6	391.7	2.4	7.1	7.5
70	2.7±0.1	322.6±2.0	29.7±1.0	354.9	2.2	6.4	6.8
80	2.0±0.1	285.0±1.8	39.3±1.4	326.3	2.3	5.9	6.3
90	1.6±0.1	253.5±1.6	48.2±1.8	303.3	2.4	5.5	6.0
100	1.3±0.1	226.8±1.5	56.2±2.2	284.3	2.7	5.1	5.8

Table 21: MAXWELLIAN AVERAGED CROSS SECTIONS AT kT=30 keV COMPARED TO PREVIOUS WORK AND EVALUATIONS

Isotope	Experiment		Evaluation	
	Cross section (mb)	Reference	Bao *et al.* [2]	Beer, Voss, Winters [30]
^{128}Xe	262.5 ± 3.7	present work[a]	248±66	347±111
	382 ± 122	Beer [12]		
^{129}Xe	617.0 ± 12.0	present work[a]	472±71	757±65
^{130}Xe	132.0 ± 2.1	present work[a]	141±51	175±49
	192 ± 54	Beer [12]		

[a] The 1.5% uncertainty of the gold cross section is not included, since it cancels out in most applications of relevance for nuclear astrophysics.

Table 20 (continued)

			^{130}Xe				
ΔE Data:	0 - 3 keV from Ref. [29][a]	3 - 225 keV this work	225 - 700 keV from Ref. [29][a]	Thermal Spectrum			
kT (keV)	I_1 (mbarn)	I_2 (mbarn)	I_3 (mbarn)	$< \sigma v>/v_T$ (mbarn)			
					stat	sys[b]	tot
8	27.3±1.4	229.7±6.8	0.0	257.0	6.9	2.8	7.4
10	18.4±0.9	212.1±5.1	0.0	230.5	5.2	2.5	5.8
15	8.8±0.4	178.8±3.1	0.0	187.6	3.1	2.1	3.7
20	5.1±0.3	156.6±2.2	0.0	161.7	2.2	1.8	2.8
25	3.4±0.2	141.0±1.7	0.1	144.5	1.7	1.6	2.3
30	2.4±0.1	129.3±1.4	0.3	132.0	1.4	1.5	2.1
40	1.4±0.1	112.5±1.1	1.6±0.1	115.5	1.1	1.3	1.7
50	0.9±0.1	100.0±0.9	4.2±0.1	105.1	0.9	1.2	1.5
52	0.8±0.0	97.8±0.9	4.9±0.2	103.5	0.9	1.1	1.4
60	0.6±0.0	89.7±0.8	7.8±0.3	98.1	0.9	1.1	1.4
70	0.5±0.0	80.7±0.7	11.8±0.4	93.0	0.8	1.0	1.3
80	0.4±0.0	72.8±0.7	15.9±0.6	89.1	0.9	1.0	1.3
90	0.3±0.0	65.9±0.6	19.8±0.8	86.0	1.0	0.9	1.3
100	0.2±0.0	59.8±0.6	23.4±0.9	83.4	1.1	0.9	1.4

[a] Normalized to present data

[b] The 1.5% uncertainty of the gold standard is not included, since it cancels out in most applications of relevance for nuclear astrophysics

References

[1] K. Wisshak, F. Voss, F. Käppeler, and G. Reffo, Phys. Rev. C **42**, 1731 (1990).

[2] Z.Y. Bao, H. Beer, F. Käppeler, F. Voss, K. Wisshak, and T. Rauscher, Atomic Data Nucl. Data Tables **76**, 670 (2000).

[3] K. Wisshak, F. Voss, C. Arlandini, F. Käppeler, M. Heil, R. Reifarth M. Krtička, and F. Bečvář, Report FZKA 6362, Forschungszentrum Karlsruhe 2000.

[4] R. Reifarth, M. Heil, M. Krtička, and F. Bečvář, Proc. Int. Symposium Capture Gamma-ray spectroscopy and related topics, Santa Fe, Bew Mexiko, 30 august - 3 september 1999, American Institute of Physics AIP conference proceedings vol 529, p 746, 2000.

[5] M. Heil, R. Reifarth, M.M. Fowler, R.C. Haight, F. Käppeler, R.S. Rundberg, E.H. Seabury, J.L. Ullmann, J.B. Wilhelmy, and K. Wisshak, Nucl. Instr. Methods **A 459**, 229 (2001).

[6] J. Apostolakis, Technical Report, CERN, GEANT library (available from: www.cern.ch).

[7] K. Wisshak, F. Voss, F. Käppeler, and G. Reffo, Phys. Rev. C **45**, 2470 (1992).

[8] K. Wisshak, K. Guber, F. Voss, F. Käppeler, and G. Reffo, Phys. Rev. C **48**, 1401 (1993).

[9] F. Voss, K. Wisshak, K. Guber, F.Käppeler, and G. Reffo, Phys. Rev. C **50**, 2582 (1994).

[10] K. Wisshak, F. Voss, F. Käppeler, K. Guber, L. Kazakov, N. Kornilov, M. Uhl, and G. Reffo, Phys. Rev. C. **52**, 2762 (1995).

[11] F. Käppeler, R. Gallino, M. Busso, G. Picchio, and C.M. Raiteri, Astrophys. J. **354**, 630 (1990).

[12] H. Beer,Astrophys. J. **375**, 823 (1991).

[13] E. Anders and N. Grevesse, Geochim. Cosmochim Acta **53**, 197 (1989).

[14] U. Ott, F. Begemann, J. Yang, and S. Epstein, Nature **332**, 700 (1988).

[15] K. Wisshak, K. Guber, F. Käppeler, J. Krisch, H. Müller, G. Rupp, and F. Voss, Nucl. Instr. Meth. A **292**, 595 (1990).

[16] P. Mutti, H. Beer, A. Brusegan, F. Corvi, R. Galleano, and A. Noriega, Proc. 10^{th} Int. Symposium *capture gamma-ray spectroscopy and related topics* Santa Fe, New Mexico 1999, AIP conference proceedings **629** 687 (2000).

[17] K. Wisshak, F. Voss, F. Käppeler, L. Kazakov, and G. Reffo, Report FZKA 5967, Forschungszentrum Karlsruhe, Karlsruhe, Germany 1997.

[18] F. Voss, K. Wisshak, C. Arlandini,K. Käppeler, L. Kazakov, and T. Rauscher, Phys. Rev. C **59**, 1154 (1999).

[19] F. H. Fröhner, Technical report, Gulf General Atomic (unpublished).

[20] A. Gilbert and A.G.W. Cameron, Can. J. Phys. **43**, 1446 (1965).

[21] J. F. Mughabghab, M. Divadeenam, and N. E. Holden, in *Neutron Cross Sections, Vol. 1, Part A* (Academic Press, New York, 1981).

[22] F. Bečvář, Proc. 10^{th} Int. Symposium *capture gamma-ray spectroscopy and related topics* Santa Fe, New Mexico 1999, AIP conference proceedings **529** 504 (2000).

[23] F. Bečvář, Nucl. Instr. Methods **A 417**, 434 (1998).

[24] G. Reffo, F. Fabbri, K. Wisshak, and F. Käppeler, Nucl. Sci. Eng. **80**, 630 (1982).

[25] R. L. Macklin, private communication (unpublished).

[26] W. Ratynski and F. Käppeler, Phys. Rev. C **37**, 595 (1988).

[27] K. Wisshak, F. Voss, and F. Käppeler, Phys. Rev. C. **54**, 2732 (1996).

[28] P.E. Koehler, J.A. Harvey, R.R. Winters, K.H. Guber, and R.R. Spencer, Phys. Rev. C. **XX**, XXX (2001).

[29] J. Kopecky, J.-Ch. Sublet, J.A. Simpson, R.A. Forrest, and D. Nierop, Report INDC(NDS)-362, International Atomic Energy Agency, Vienna, Austria, 1997.

[30] H. Beer, F. Voss, and R.R. Winters, Astrophys. J. Suppl. **80**, 403 (1992).